INSTITUTO SUPERIOR TÉCNICO
Universidade Técnica de Lisboa

SPACE SUIT SIMULATOR

DEVELOPMENT PROJECT

Develop, Test and Model a Space Suit Simulator

Knee joint

Ivo Miguel Lopes Ferreira

Dissertação para a obtenção do grau de mestre em

Engenharia Aeroespacial

Júri

Presidente: Prof. Carlos Jorge Ferreira Silvestre

Orientação: Prof. Alexandra S. Gonçalves Aguiar Gomes

Vogais: Prof. Paulo Jorge Soares Gil

October 2007

Acknowledgments

This thesis was completed between May and August 2007 at the MVL (Man Vehicle Laboratory), a laboratory of the MIT (Massachusetts Institute of Technology).
I would like to express my more sincere gratitude to Prof. Dava Newman which agreed to ensure the responsibility for my internship and which, especially, by her advices and assistance, guided me throughout the thesis.

My thanks also go for the other elements of the team which took part and will continue taking part of the S3 project at the MIT, Jessica Marquez, Jessica Edmonds and Junjay Tan. It was an enormous pleasure to work with intelligent and gifted people like you guys.

I would also like to thank the other partners of the project, Dr. Grant Schaffner of NASA/JSC, Mr. Keith van der Walde and Mr. Douglas Moore of the ATA, by the excellent co-operation and guidance in many teleconferences.

My recognition also goes to the whole members of the MVL who, for four months, contributed to my insertion within the laboratory.

Finally, I am thankful to my family for having provided me with the conditions for developing during my life. I am thankful to my friends as well, to those who came and those who went, for I couldn't have done it without you.

Resumo

Os momentos requeridos para mover as articulações de um fato espacial são funções não-lineares complicadas que mudam com a posição e a velocidade do deslocamento da articulação. A incerteza no conhecimento destes momentos conduz a grandes variações nos custos metabólicos do astronauta e reduz o desempenho da EVA.

Esta é a razão porque hoje, sejam os verdadeiros fatos espaciais a ser utilizados para o planeamento deste tipo de actividades.

O uso do simulador para o planeamento de EVAs permitirá uma redução dos custos do planeamento, uma simplificação do treino dos astronautas e um melhor estudo da influência dos vários parâmetros de um fato espacial no comportamento do astronauta.

Esta tese descreve o procedimento que permitiu a caracterização da articulação do joelho de um simuador de fatos espaciais em termos da sensibilidade à velocidade do deslocamento, à gama de ângulos, à fricção e à rigidez.

Finalmente, para melhor compreender o efeito de uma mudança na rigidez da articulação, um modelo físico foi construído. Para prever o efeito do comportamento histerético da articulação, um novo modelo matemático, baseado no modelo de Bouc-Wen foi construído.

Palavras chave: Fato espacial, EVA, Aquisição de dados, Histerése, Bouc-Wen

Abstract

The torques required to move the joints of a spacesuit are complicated nonlinear functions changing depending on the position and the displacement speed of the joint. Uncertainty in the knowledge of these torques leads to great variations of the metabolic costs of the astronaut and thus, reduces the performance of the EVA.

This is the reason why currently the real spacesuits are used for planning this type of activities.

The use of a simulator to plan EVAs will allow a reduction of the planning procedures costs, a simplification of the training procedure of the astronauts and a better study of the influence of the various parameters of a spacesuit on the behavior of the astronaut.

This thesis describes the procedure that allowed the characterization of the knee joint of this simulator in terms of the sensitivity to the displacement speed, angle range, friction and stiffness. To better understand the effect of a change on the joint stiffness, a physical model of the joint was built. Also, to predict the hysteretic behavior of the joint, a new model, based on the Bouc-Wen model was built.

Keywords: Spacesuit, EVA, Data Acquisition, Hysteresis, Bouc-Wen

Contents

ACKNOWLEDGMENTS II

RESUMO III

ABSTRACT IV

CONTENTS V

LIST OF ACRONYMS VIII

CHAPTER 1 - INTRODUCTION 1

1.1 The MVL 1

1.2 Context and motivation 3

1.3 Project 4

CHAPTER 2 - TESTING TOOLS 6

2.1 Background 6

2.2 The Robotic Space Suit Tester (RSST) 6

2.2.1 Improvements in the control system 9

2.3 Choice of the Data Acquisition Boars (DAQ) 9

2.4 Software to interface with the robot 10

2.4.1 Interface with data acquisition boards (DAQ) 10

2.4.2 Control System 12

2.4.3 Final Configuration 13

2.5 Robot calibration 14

2.5.1 Calibration of the position of each joint 14

2.5.2 Calibration of the torque of each joint 15

2.6 New graphical user interface (GUI) **15**

CHAPTER 3 - DATA ANALYSIS AND TREATMENT **17**

3.1 Load Trajectories **17**

3.1.1 Trajectories to generate mathematical model 18

3.2 Data Filtering **19**

3.3 Remove torque generated by weight of the robot **20**

3.3.1 Detection of transition phase 20

3.3.2 Scaling procedure 21

CHAPTER 4 - TEST CONFIGURATION **23**

4.1 Knee joint of the space suit simulator **23**

4.2 Knee joint installation on the robot **24**

4.3 Testing procedure **24**

4.4 Data Filtering and processing **25**

CHAPTER 5 - RESULTS **26**

5.1 Sensitivity of the joint torque versus angle relationship to joint displacement speed ... **26**

5.2 Sensitivity of the joint torque versus angle relationship to the **27**

limitation of the joint range of motion **27**

5.3 Sensitivity of the joint torque versus angle relationship to the friction adjustment **28**

5.4 Sensitivity of the joint torque versus angle relationship to the **29**

stiffness **29**

5.5 Sensitivity of the joint torque versus angle relationship to the **30**

Preload **30**

5.7 Energy Loss **33**

5.7.1 Method to calculate energy loss 33

5.7.2 Energy Loss results 34

CHAPTER 6 - MODELS 37

6.1 Physical Model 37
6.1.1 Methods 37
6.1.2 Spring Deflection 39
6.1.3 Spring's force 40
6.1.4 Torque generated by the springs 41
6.1.5 Results of the physical model 42
6.1.6 Final comments on the physical model 43

6.2 Mathematical Model 44
6.2.1 Hysteretic behavior 44
6.2.2 Bouc-Wen model 45
6.2.3 Bouc-Wen model application to our results 46
6.2.4 Results of the mathematical model 48
6.2.5 Final comments on the mathematical model 49

CHAPTER 7 - CONCLUSION 50

BIBLIOGRAPHY 51

APPENDIX A: EXPERIMENTAL PROTOCOL AND TEST MATRIX 52

Description of Test Parameters 54
Trajectory 54
Speed 54
Range of Motion (ROM) of the Brace 55
Range of Motion (ROM) of the Robot: 55
Friction 56
Stiffness 56
Pre-load 56
EMU comparison 56
Calibration 57
Repeatability 57
To ensure repeatability, ATA also specified torque values for tightening the knee brace bolts, which we adhered to. They were as follows: 57
Data Collection 57

APPENDIX B: HYSTERESIS PLOTS 58

List of Acronyms

ATA - ATA Engineering Inc.
DAQ - Data Acquisition
EMU - Extra-Vehicular Mobility Unit
EVA - Extravehicular Activity
GUI - Graphic User Interface
ISS - International Space Station
JSC - Johnson Space Center
M2R - Masters to Research
MCP - Mechanical Counter Pressure
MIT - Massachusetts Institute of Technology
MKI - MIT Kavli Institute
MVL - Man Vehicle Laboratory
NASA - National Air and Space Administration
PCI - Peripherical Component Interconnect
RSST - Robotic Space Suit Tester
RSSTA - Robotic Space Suit Tester Adaptor
S3 - Space Suit Simulator
USB - Universal Serial Bus

CHAPTER 1 - Introduction

Even though this thesis was done to achieve a Masters degree in Aerospace Engineering at Instituto Superior Técnico – Lisbon, Prof. Alexandra S. Gonçalves Aguiar Gomes was only advisor for administrative purposes.

1.1 The MVL

The Man Vehicle Laboratory (MVL) at the Massachusetts Institute of Technology is located within the MIT Kavli Institute for Astrophysics and Space Research (MKI).
Founded in 1962, MVL's goal is to better define the physiological and cognitive limitations of pilots and passengers of aircraft and spacecraft, and to optimize overall human-vehicle system effectiveness and safety. Research is interdisciplinary, utilizing techniques from manual and supervisory control, estimation, signal processing, biomechanics, cognitive psychology, artificial intelligence, sensory-motor physiology, human factors, and biostatistics. Students are from the Department of Aeronautics and Astronautics, and also the Departments of Electrical Engineering and Computer Science and Mechanical Engineering, and the Harvard-MIT Division of Health Science and Technology.

Here is a synthesis of MVL's current research topics:

- Visual orientation – human adaptation to a space environment (where there isn't a "gravitational reference");

Figure 1 - Exercise in a Treadmill with springs to simulate gravity

Figure 2 - Use of a virtual reality tool for astronauts' orientation

- Spatial Memory: Mechanisms and Countermeasures – development of tools to help with astronauts' navigation in the International Space Station (ISS); study of the influence of the position of the cameras to control the robot mechanical arm in the ISS ("*Canadarm*");

- Locomotion Modeling and Orthoses;

Figure 3 - Control station of the robot mechanical arm in the ISS

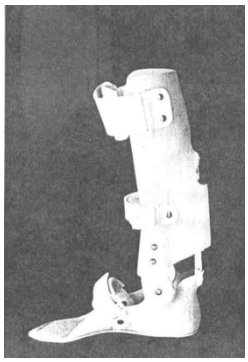

Figure 4 - Example of an Orthosis

- Adaptation to Artificial Gravity– use of a centrifuge to study the effect of a lot of parameters in the human vestibular system

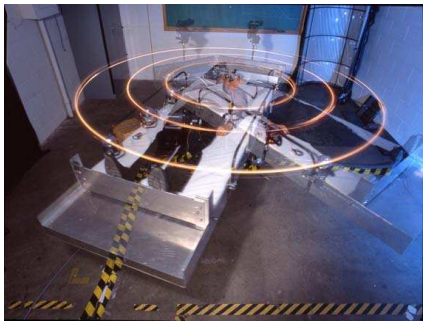

Figure 5 - Centrifuge used for the studies

- Research in the field of extravehicular activities – development of the spacesuit concept (« *Biosuit Project* ») with a *Mechanical Counter Pressure concept* (MCP), *Space Suit Simulator* (S3)

Figure 6 - Robot used to test spacesuits with the EMU (present spacesuit used on the space shuttle)

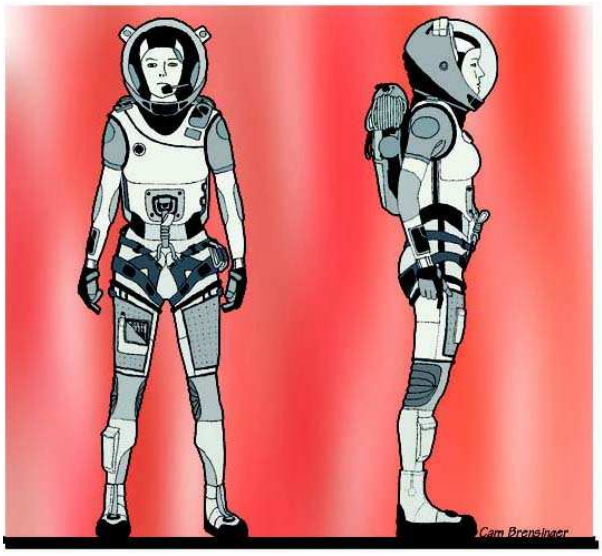

Figure 7 - Concept of a new spacesuit « Biosuit Project »

- "*Mars Gravity Biosatellite*", satellite used to study in orbit the effects of Martian gravity on mammals.

Figure 8 - Logo of the « Mars Gravity » Mission

1.2 Context and motivation

Astronauts and cosmonauts have made great accomplishments while working outside of their spacecraft, assembling and maintaining space stations, capturing and repairing satellites and even exploring the Moon [8].When astronauts exit their spacecraft to perform extravehicular activities, or EVA's, these operations carry extremely high costs in time, money, risks to personnel, and limited opportunities. Because of the high costs of EVA and the importance of accomplishing planned objectives, months of prior planning and hundreds of hours of rehearsal are required to prepare for each EVA. Planning for EVA's is complicated by the fact that it is not possible to exactly replicate the microgravity, vacuum environment in a single simulation environment on the ground. Thus, successful planning for EVA's requires accurate knowledge of the EVA environment and the capabilities of an astronaut wearing a spacesuit [3].

The number of EVAs increases since the beginning of the space race, and the tendency is to continue increasing.

The following figure compares the number of extravehicular activities carried out by the American and the Russian space program from 1965 to 2000 with the number of expected extravehicular activities in a human mission at Mars:

Figure 9 - Evolution of the number of EVAs[3]

Note: The number for the human mission to Mars was found by considering 600 days of stay for a four members' crew with roughly two extravehicular activities per week (a low evaluation of what will be a possible mission to Mars).[2]

The purpose of this thesis is to unify and generalize spacesuit mobility performance measures by modeling the fundamental relations that govern spacesuit performance, specifically, the constitutive relations between joint displacements and applied torques.
Understanding the fundamental relationships governing spacesuit performance provides a basis for predicting a global performance measure using information about another performance measure, for instance, predicting a reach envelope using range of motion data. This insight will allow performance measures to be generalized to alternative scenarios, such as determining work envelopes for different-sized crew members.

1.3 Project

The NASA Johnson Space Center Exercise Countermeasure Project and EVA Physiology Systems and Performance Project are developing a Space Suit Simulator (S3) to substitute for an actual spacesuit during certain types of tests and experiments. The space suit simulator is intended to replicate the mechanical properties of a spacesuit, in terms of resistance to motion and mass and inertia, but without the requirements for pressurization or thermal regulation. This capability will provide several advantages over testing with an actual spacesuit:

1. Reduces cost by eliminating the need for support personnel and consumables associated with actual spacesuits.
2. Eliminates the cost and programmatic impact associated with consumption of suit life due to high cycle testing.
3. Simplifies scheduling since suit simulators will be more readily available than actual spacesuits.
4. Facilitates the use of instrumentation (e.g., metabolic gas analysis, electromyography) that is otherwise difficult or infeasible to implement when using an actual spacesuit.
5. Allows for variation of suit properties to assess the impacts of specific suit parameters (e.g., suit mass, joint resistance, etc.)

The concept that is proposed for the space suit simulator is an exoskeleton-type suit that utilizes commercial-off-the-shelf joint braces, to which are added passive resistance elements, such as bungees and springs, and mass elements that provide the required resistance to motion. The suit joints will be linked-together in a kinematic chain that matches that of the human body using adjustable frame elements. The complete suit will include the following 10 joints with associated degrees of freedom:

- 2 ankle joints, allowing 3 degrees of freedom (rotation, inversion and flexion)
- 1 knee joint, allowing 1 degree of freedom (flexion)

- 2 hip joints, allowing 3 degrees of freedom (flexion, abduction and rotation)
- 1 torso joint, allowing 1 degree of freedom (rotation)
- 2 shoulder joints, allowing 3 degrees of freedom (rotation, flexion and abduction)
- 1 elbow joint, allowing 1 degree de freedom (flexion).

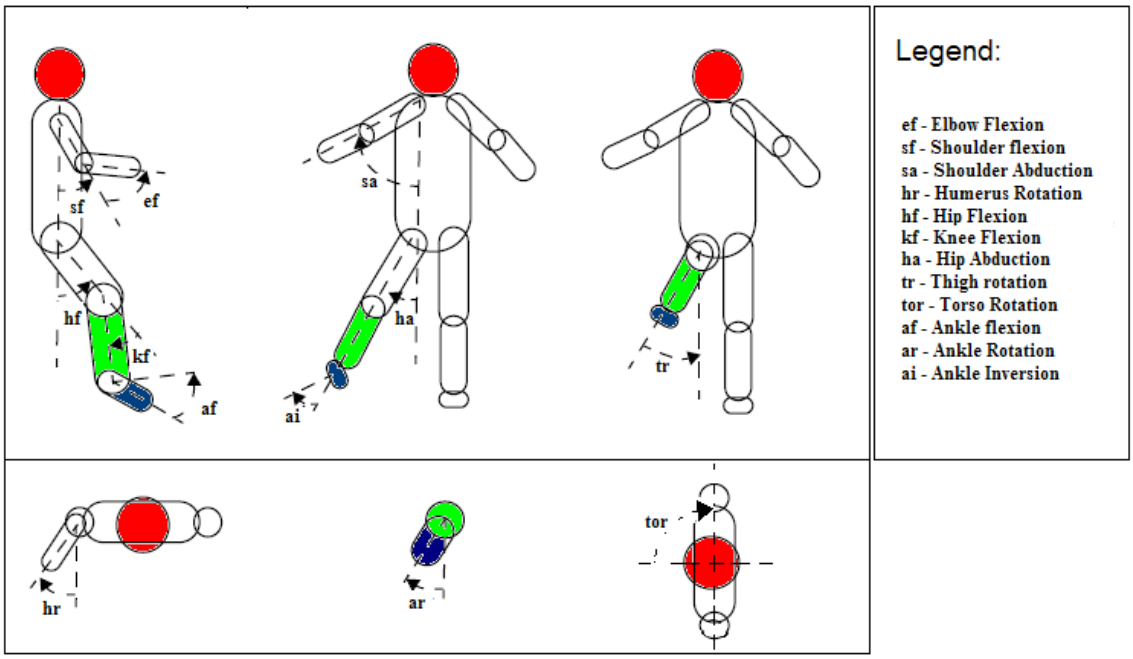

Figure 10 - Different degrees of freedom associated with the different joints

This project is divided in four phases related to the development and test of the space suit simulator:

- Phase I - Knee Joint
- Phase II - Add ankle and hip to complete right leg, plus lower torso
- Phase III - Shoulder and elbow for right arm, plus upper torso
- Phase IV - Complete opposite side arm and leg and integrate complete suit

The job of the MIT is, at each step, to test, model and validate the design of the simulator.
This thesis describes the procedure developed do arrive to this goal and reveals the first results for the Phase I of the project (knee joint).

CHAPTER 2 - Testing tools

2.1 Background

Since the first extravehicular activities in 1965, the capabilities of EVA astronauts to do useful work outside of their spacecraft have steadily progressed. Likewise, our understanding of EVA's capabilities and limitations on the astronauts have also progressed through in-flight experience, experimentation in neutral buoyancy and parabolic flight, and engineering tests of spacesuits and EVA tools[2].

Computer models and dynamic simulation are the most recent tools for analyzing EVA capabilities. Computer simulation of EVA has several advantages over physical simulations, including the ability to accurately reproduce forces and displacements in six degrees of freedom and the absence of inherent time and workspace limitations.

One important shortcoming of current EVA models is that they lack an accurate representation of the torques that are required to bend the joints of the spacesuit. Modern spacesuits are designed to move with astronauts, using bearings and constant-volume joints to minimize resistance to motion [5]. However, the torques required to perform EVA tasks still have a significant impact on task performance. The torques required to move spacesuit joints are complicated nonlinear functions of joint position and rate. Uncertainty in the knowledge of these torques leads to large variations in predicted task performance and metabolic costs.

This problem forced NASA to launch, in the 90's, a project for the development of a robot with the same essential degrees of freedom of a human person to be able to measure in an exact way the torques required for various configurations of positioning and rate of travel of the articulations. [4]

2.2 The Robotic Space Suit Tester (RSST)

The company which won the contest for the construction of the robot was *Sarcos Inc.* (Salt Lake City, UT, USA).
The robot, that is called "Robotic Space Suit To test" (RSST) or simply Mr. Tallchief to honor the most important ballerina of the American history, was lent to MIT by NASA in 1998 for the research of the mobility of the EMU (spacesuit used in the Space Shuttle)[7]. This robot remained with the MVL until today to develop new tools for its use and to test future spacesuits.
The RSST, shown in

Figure 13, is an anthropomorphic robot whose primary purpose is to measure the joint torques exerted by a spacesuit on a human wearer.
The RSST has 12 hydraulically actuated joints on the right arm and 12 poseable joints on the left arm and leg. At each actuated joint, potentiometers measure joint deflection and strain gauge load cells measure torque.

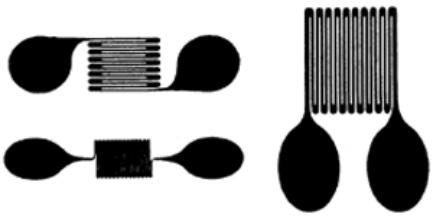

Figure 11 - Examples of strain gauge load cells (devices used to measure deformation (strain) of an object)

Figure 12 - Sensor, integrated in the robot joints, used to measure the torques

The actuated joints of the robot are powered by an MTS model 510 hydraulic pump.
Hydraulic fluid circulates in a loop from the pump, through each robot joint actuator, then back to the pump.
The next picture shows the different joints of the robot:

Figure 13 - Joints of the RSST

Number	Description
1	Shoulder Flexion
2	Shoulder Abduction
3	Humerus Rotation
4	Elbow Flexion
5	Wrist Rotation
6	Hip Flexion
7	Hip Abduction
8	Thigh rotation
9	Knee Flexion
10	Ankle Rotation
11	Ankle Flexion
12	Ankle Inversion

Table 1 - Description of the different joints of the RSST

Sarcos supplied the robot as well as a set of hydraulic controller boards that are controlled either analogically or digitally by an old 386 computer. Additionally, NASA developed a Robot Space Suit

Tester (RSSTA) software program that could be run in Windows 3.1 to input trajectories and output torque and joint angle values through a graphical user interface. RSSTA runs on a 486 computer that is linked to the 386 computer through a VMEbus.

Figure 14 - Connection to the VME, VMEBus

The hydraulic boards execute a complex control system (Figure 15), defined by a low gain PD controller with a torque feedback, but the graphical interface to control these boards is very difficult to run and modify.

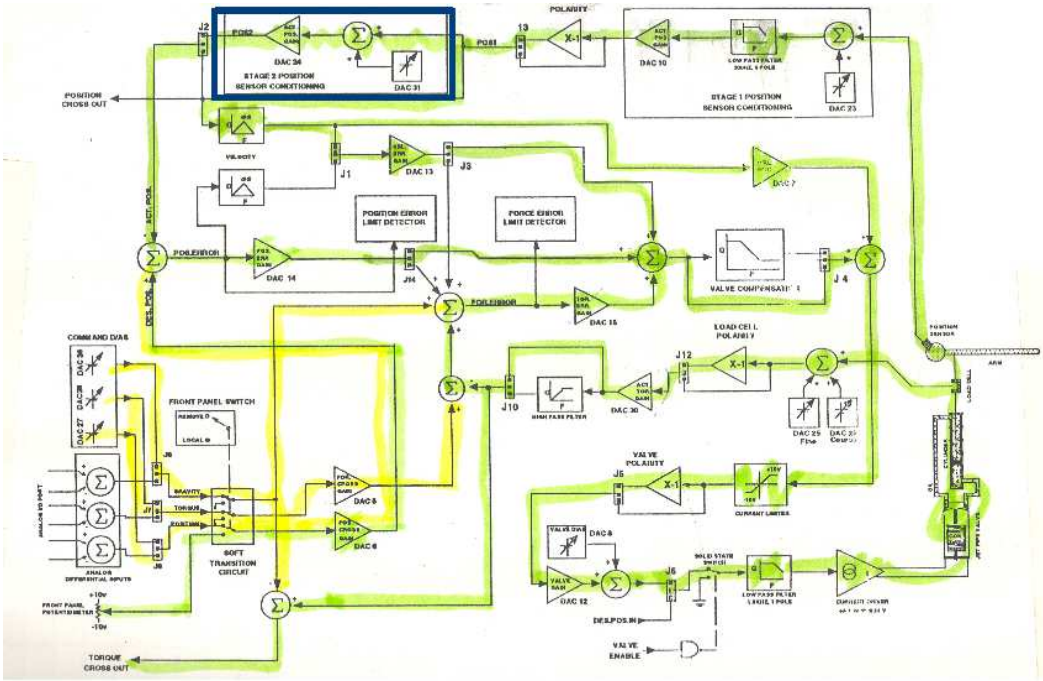

Figure 15 - Control System of the Hydraulic Boards

Note: The yellow loop represents the command loop; the green loop represents the control loop itself.

The robot input may be done by digital inputs using the “mother board” of the VME or by analog inputs (±10V) connected to the VMEBus (Figure 14).

In the same way, the telemetry of joint position and torque may be received by the “mother board” or can be exported as an analog output (±10V).

2.2.1 Improvements in the control system

There were several factors which led to an improvement of the robot’s control system, namely:

- The lack of robustness, which was initially made by a software installed on a computer with a processor 486 (which allowed a maximum frequency of 5 Hz);
- The limitation of the existing graphical interface;
- And more importantly, the difficulty in analyzing the data.

The idea was therefore to concatenate the control system in only one computer which could design the trajectories of the robot, load the gains and then, analyze the data given with a good user friendly graphical interface.
The basic plan was to build the controllers on Simulink - Matlab and then to use the Data Acquisition Toolbox (DAQ Toolbox) to convert the trajectories given by the user into analog inputs which could be read by the VME.
The following sub-sections describe the modifications which were required to do so.

2.3 Choice of the Data Acquisition Boars (DAQ)

After an exhaustive evaluation of the existing products in the market and a “philosophy” to remain within the budget of the project, two boards were selected to control the 12 joints of the robot simultaneously.
The majority of the boards that exist today still use connections PCI because they allow data transfer speed much higher than USB connections. But for the necessary number of channels, 12 channels of analogical output (to control the position of the joints) and 24 analog channels of input (to have the telemetry of the real position of each joint and the respective torques), the PCI technology presented prohibitive prices.
Thus, the selected connection was USB and the acquired boards were of two distinct companies:

- Data Translation DT9814-10V, having 24 analogical inputs with a resolution of 12 bits with a frequency of 50 KHz; and,

- Measurement Computing USB-3105, having 16 analogical outputs with a resolution of 16 bits with a frequency of 100 Hz.

2.4 Software to interface with the robot

2.4.1 Interface with data acquisition boards (DAQ)

The choice of the use of Matlab, in particular Simulink, allowed the use of the DAQ Toolbox. This tool transformed the integration of the boards in an easy task because there were already "blocks" to represent the various inputs and outputs of the boards in a model of Simulink.

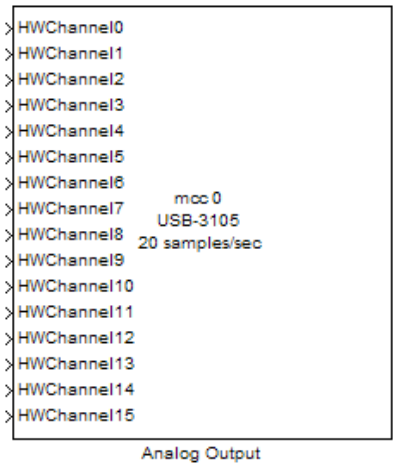

Figure 16 - Example of a Simulink "block" representing the analog output of the board USB-3105

The only thing missing was a control system and an interface between the user-defined trajectories and the analog outputs.
For this a Simulink model was developed to linearly transform a position in a voltage (according to the maximum/minimal range of the joint and maximum/minimal voltage of the outputs) in the following way:

$$Voltage\_ouput\ \ (Position) = Minimum\_Voltage + \frac{Position - Minimum\_Position}{Maximum\_Position - Minimum\_Position} \times \left(Maximum\_Voltage - Minimum\_Voltage\right)$$

Equation 1

Where the *Position* is the angular position of the joint, *Voltage_output* is the analog output to send to the VME (through the data acquisition boards).

Minimum_Voltage and *Maximum_Voltage* are: -10 and +10 V, respectively.

The values of the *Minimum_Position* and *Maximum_Position* depend on the considered joint:

Number	Description	*Minimum_Position(º)*	*Maximum_Position(º)*
1	Shoulder Flexion	-15	180
2	Shoulder Abduction	0	90
3	Humerus Rotation	-90	90
4	Elbow Flexion	0	130
5	Wrist Rotation	-90	90
6	Hip Flexion	0	100
7	Hip Abduction	0	45
8	Thigh rotation	-22	22
9	Knee Flexion	0	130
10	Ankle Rotation	-20	20
11	Ankle Flexion	-45	30
12	Ankle Inversion	-20	20

Table 2 - Angle ranges for the different joints of the robot

In the same way, for the telemetry analysis:

$$Position\ (Voltage\_Position\_Input) = Minimum\_Position + \frac{Voltage\_Position\_Input - Minimum\_Voltage}{Maximum\_Voltage - Minimum\_Voltage} \times \left(Maximum\_Position - Minimum\_Position\right)$$

Equation 2

And,

$$Torque(Voltage\_Torque\_Input) = Minimum\_Torque + \frac{Voltage\_Torque\_Input - Minimum\_Voltage}{Maximum\_Voltage - Minimum\_Voltage} \times \left(Maximum\_Torque - Minimum\_Torque\right)$$

Equation 3

Where, *Voltage_Position_Input* and *Voltage_Torque_Input* are the analog inputs sent by the VME through the data acquisition board.

The values of the *Minimum_Torque* and *Maximum_Torque* depend on the considered joint:

Number	Description	*Minimum_Torque(N.m)*	*Maximum_Torque(N.m)*
1	Shoulder Flexion	-45,2	39,6
2	Shoulder Abduction	-45,2	39,6
3	Humerus Rotation	-28,3	28,3
4	Elbow Flexion	-39.6	31
5	Wrist Rotation	-102	56,5
6	Hip Flexion	-147	147
7	Hip Abduction	-45,2	226
8	Thigh rotation	-56,5	56,5
9	Knee Flexion	-84,8	84,8
10	Ankle Rotation	-56,5	56,5
11	Ankle Flexion	-79,1	79,1
12	Ankle Inversion	-56,5	56,5

Table 3 - Torque ranges for the different joints of the robot

Here is a screenshot of the Simulink model to establish the process described by **Equation 1, 2 and 3**.

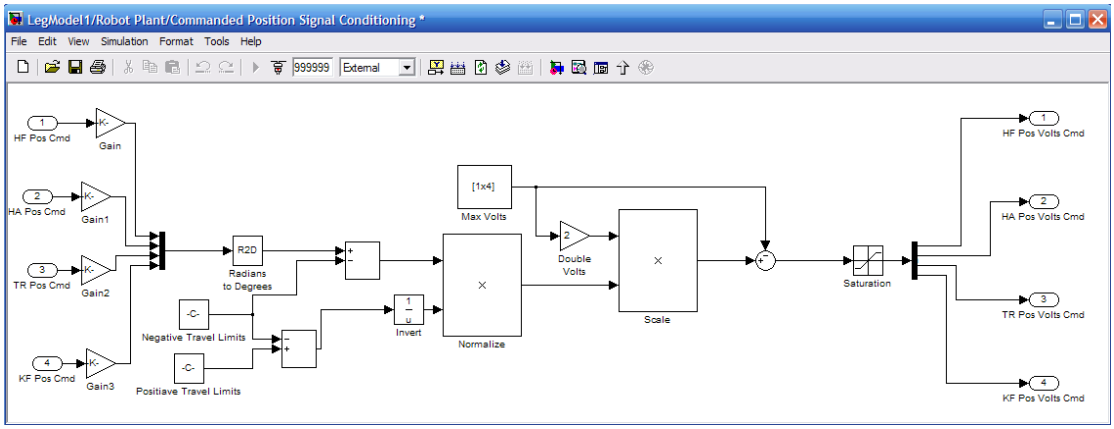

Figure 17 - Screenshot of the Simulink model

Note: This figure only represents the conversion of the input command into an analog input

2.4.2 Control System

It was noticed that internal PD controller of the hydraulic boards (Figure 15) was sufficient to control the system.

As it can be seen on Figure 18, the only differences between the input command of position and the output position, after calibration (Pag. 14), was a delay of roughly 0.2 seconds and a small difference close to the maximum and minimal positions.

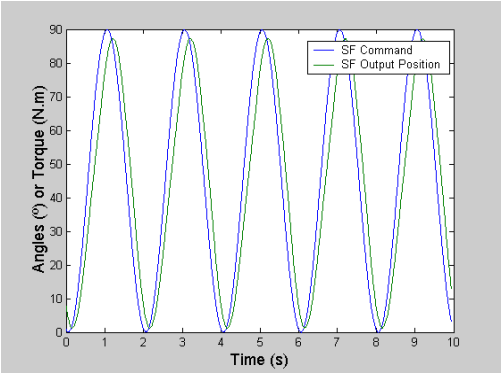

Figure 18 - Output of one joint (Shoulder Flexion) to a sinusoidal input

Moreover, looking at the output of a step input (Figure 19), it can be noted that the complete system (controller + joint) has a first order type response with a time-constant of 0.2 s, as shown on Figure 18.

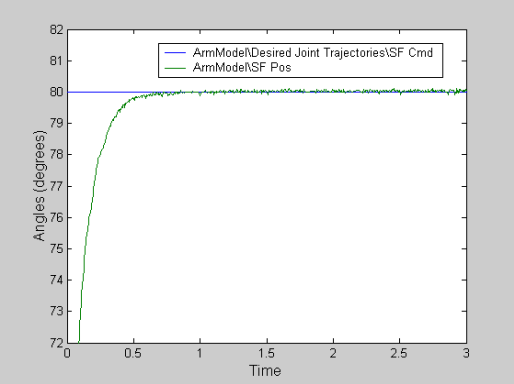

Figure 19 - Output of one joint (Shoulder Flexion) to a step input

Since the response of the system satisfied our requirements, there was no need to establish a new controller in the Simulink model.

2.4.3 Final Configuration

The next figure shows the final software configuration developed to control the robot:

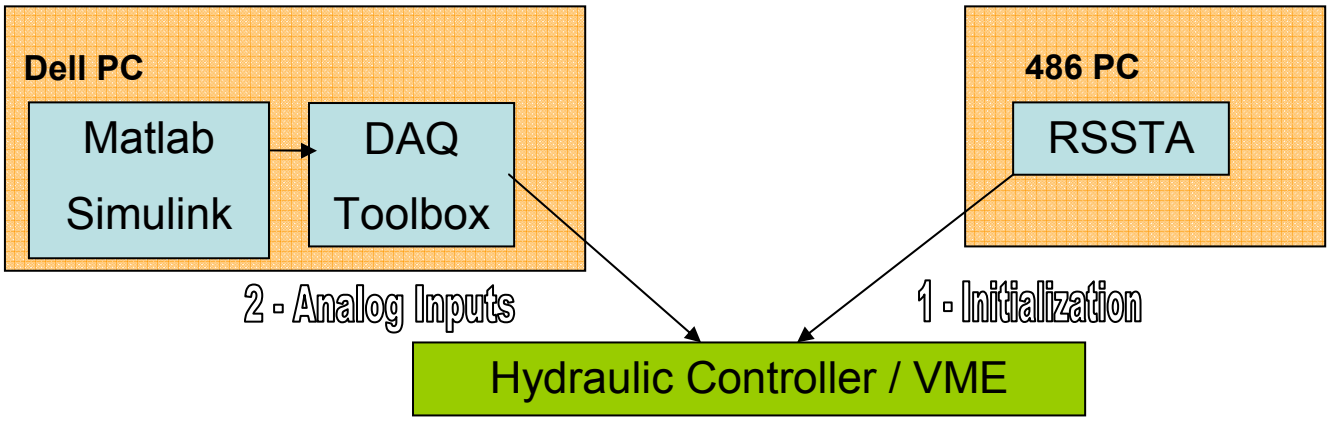

Figure 20 - Final software configuration used to control the robot

Where « Dell PC » is the computer that holds the Simulink model which allows the generation of analog inputs to control the robot.
Unfortunately, the old computer could not be “bypassed”. It had to be used to the initialization process of the hydraulic boards (through the RSSTA interface), but all the other processes to control and analyze the telemetry were done using « Dell PC ».

2.5 Robot calibration

The calibration of the robot was done by using tables (“Look up Tables”), since it was the best way to consider the nonlinear effects. It was also advantageous to do it this way to avoid the definition of the various offsets and gains for each joint.

2.5.1 Calibration of the position of each joint

Figure 21 - Calibration of the position of the arm joints

We used a simple procedure to calibrate joint angles. First, we labelled angle values on the robot joints using masking tape. Next, we input a simple angle (α_{input}) and observed the corresponding result in the robot (α_{real}) and the output shown on the computer (α_{output}). After that it was only necessary to invert the relations:

- the first look-up table (before sending signals to the robots) had as an input α_{real} and has an output α_{input} , and;
- the second look-up table (after receiving signals to the robots) had as an input α_{output} and has an output α_{real}.

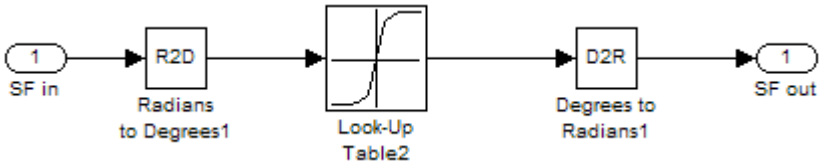

Figure 22 - Example of the « Look up Table » used in the Shoulder Flexion joint

2.5.2 Calibration of the torque of each joint

Figure 23 - Calibration of the torque of the arm joints

To calibrate the torque outputs, the procedure was basically the same as the one used to calibrate joint positions.

We input external torque by means of constant force springs and then examined the output torque shown in the computer ($torque_{output}$). Next, we built a look-up table as done before for the calibration of each joint position. Since we had no information about the robot's own mass, torque calibration was performed in a way such that the angle was constant and the torque generated by the robot itself was zero (i.e. the gravity vector was aligned with the robot limb segment).

2.6 New graphical user interface (GUI)

Finally, in order to integrate all the code developed in Matlab in a platform of easy use by the user, a new graphical interface was developed. Here are some screenshots of this tool:

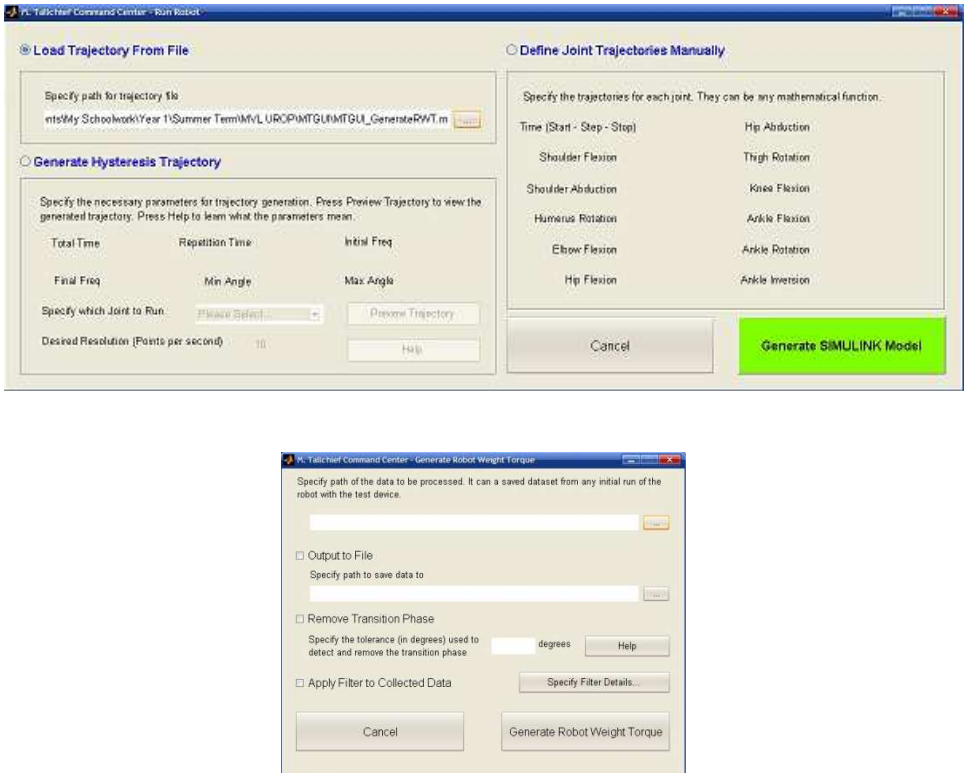

Figure 24 - Screenshots of the new GUI

CHAPTER 3 - Data analysis and treatment

The goal of this phase was to start analyzing the data coming out of the robot (after the real time software installed on the Dell's computer).
Several scripts were built to analyze and process the data from the robot so that the real hysteresis graphs from each joint could be obtained. A simple description of each script follows.

3.1 Load Trajectories

There is a simple script that concatenates all the possibilities to load trajectories, described below.

- **init_robot.m**. This script initializes all the parameters for the Simulink model (including the calibration parameters) and allows the user to choose the trajectory to be loaded into the robot.
The user can either create a **user-defined trajectory** for each joint, **load human trajectory** files used by Schmidt[7] (for comparison purposes) or, input parameters that will **generate trajectories for hysteresis graphs with different ranges of motion**, like those shown in Figure 25.

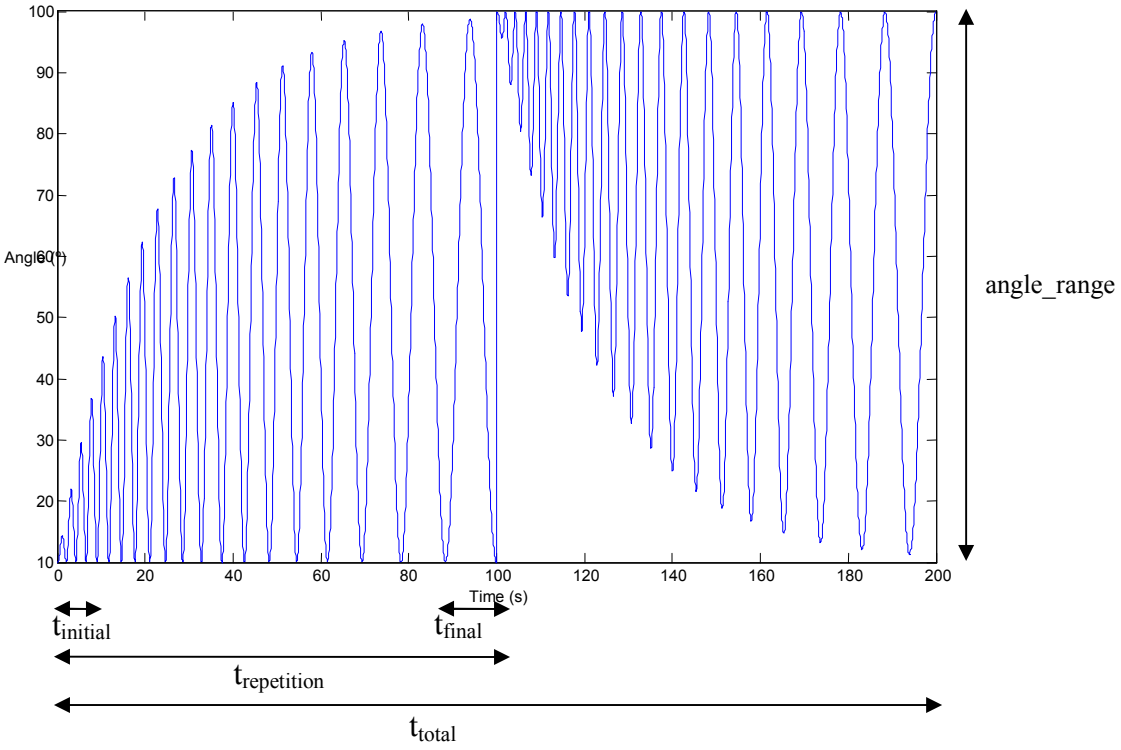

Figure 25 - Example of trajectory to generate mathematical model

3.1.1 Trajectories to generate mathematical model

In these trajectories, the user can define the maximum and minimum angles (**angle_range**), the total time of simulation ($\mathbf{t_{total}}$), the resolution time, the repetition time ($\mathbf{t_{repetition}}$), the initial period and final period ($\mathbf{t_{final}}$).

These trajectories were defined mathematically using an exponential function multiplied by a periodic function with a changing period.

The properties of the exponential were found by the fact that at the repetition time the angle should be at the maximum value, i.e.:

$$Max\_angle - Min\_angle = e^{\alpha t_{repetition}} \text{ , so,}$$

$$\alpha = \frac{\ln(Max\_angle - Min\_angle)}{t_{repetition}} \text{ , and,}$$

$$f_1(t) = e^{\frac{\ln(Max\_angle - Min\_angle)}{t_{repetition}} t}$$

Equation 4

Since the frequency of the periodic function varies from an initial period to a final period, a linear function was built to express the period at each time:

$$Period(t) = t_{final} * \frac{t}{t_{repetition}} + t_{initial} * \frac{(t_{repetition} - t)}{t_{repetition}}$$

Equation 5

Also, since the desired periodic function should only have positive values, the chosen function was a $\cos^2(...)$. So, since the period of a $\cos^2(...)$ is two times the period chosen by the user:

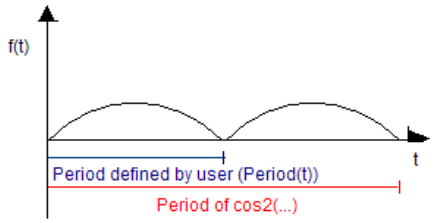

So, $$f_2(t) = \cos^2\left(\frac{\pi}{t_{final} * \frac{t}{t_{repetition}} + t_{initial} * \frac{(t_{repetition} - t)}{t_{repetition}}} t\right)$$

Equation 6

The final trajectory is defined by:

$$y(t) = Min\_Angle + f_1(t) * f_2(t),$$

$$y(t) = Min\_Angle + e^{\frac{\ln(Max\_angle - Min\_angle)}{t_{repetition}} t} \cos^2\left(\frac{\pi}{t_{final} * \frac{t}{t_{repetition}} + t_{initial} * \frac{(t_{repetition} - t)}{t_{repetition}}} t \right)$$

Equation 7

3.2 Data Filtering

The data output from the robot is very noisy, so there was a need to apply a filter before plotting each result. The script that allows this feature is described below.

-**Data_Analysis.m**. Through this script the user can chose from two types of filters to apply to his data, either a Chebyshev or a Butterworth filter, chose the order of the filter, the data to which apply the filters and the cut frequency of the filter.

The choice of the type of filter is up to the user.

The Butterworth is designed to have a frequency response that is as flat as mathematically possible in the passband. The Chebyshev filters have a steeper roll-off and more passband ripple than Butterworth filters but have the property of minimizing the error between the idealized filter characteristic and the actual over the range of the filter, but with ripples in the passband.

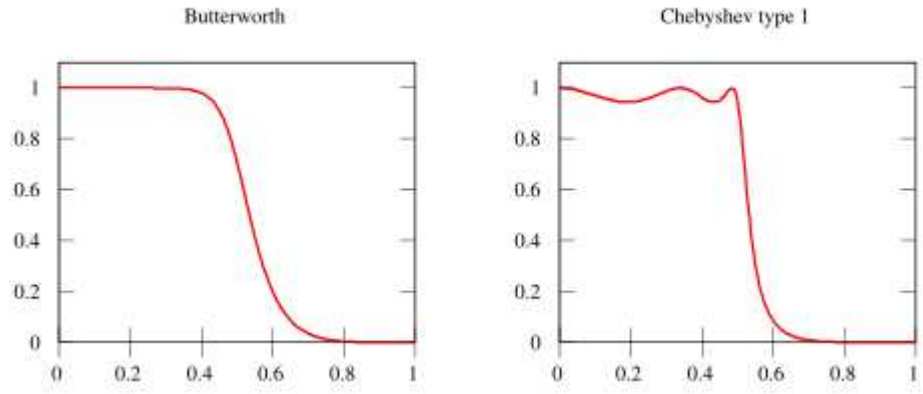

Figure 26 - Differences between the response of a Butterworth and a Chebyshev filter (with normalized cut-off frequency=0.5)

Figure 27 is an example of the application of a Butterworth filter (order 10, 10 % cut-off frequency) to the actual data from the robot (Knee flexion torque).

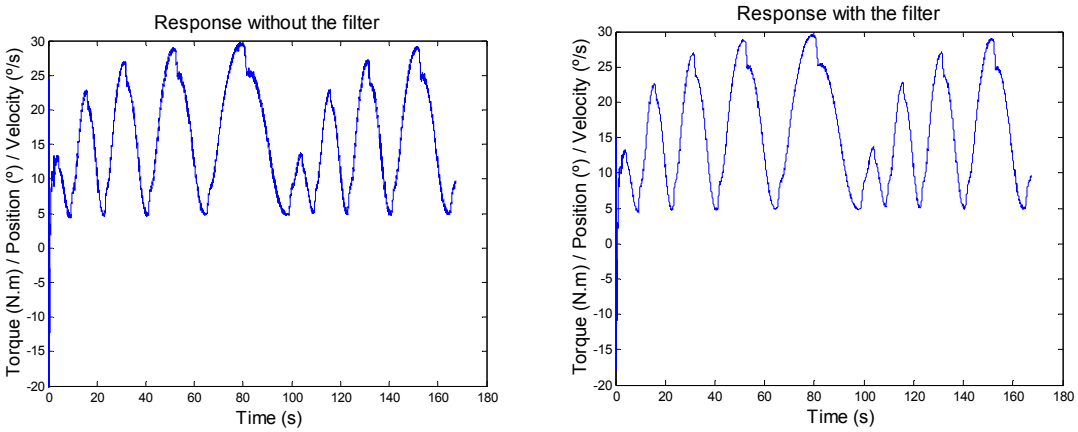

Figure 27 - Example of the effect of the filtering process

Note: The cut-off frequency of the input in this script is the ratio of the real cut-off frequency and the maximum frequency of the signal (that is defined as ½ the padding frequency – according to Shannon's law).

3.3 Remove torque generated by weight of the robot

In order to measure the effect the spacesuit simulator has on the joints, the torque generated by the robot's weight needs to be subtracted from the raw robot output data. This is not a straight-forward task nor could Schmidt's methods be replicated (as she used a different method to control the robot and acquire data).

3.3.1 Detection of transition phase

The only way to synchronize the torque and angles was to start recording from the beginning of the trajectory.

The sensors have a transitory phase that has to be identified and eliminated. This was accomplished by comparing the input trajectory with the output position and searching the point where the difference between these two functions was within five degrees. This was done by comparing three different points after the possible point of transition: when all these points where within that margin, then the transition point had been reached.

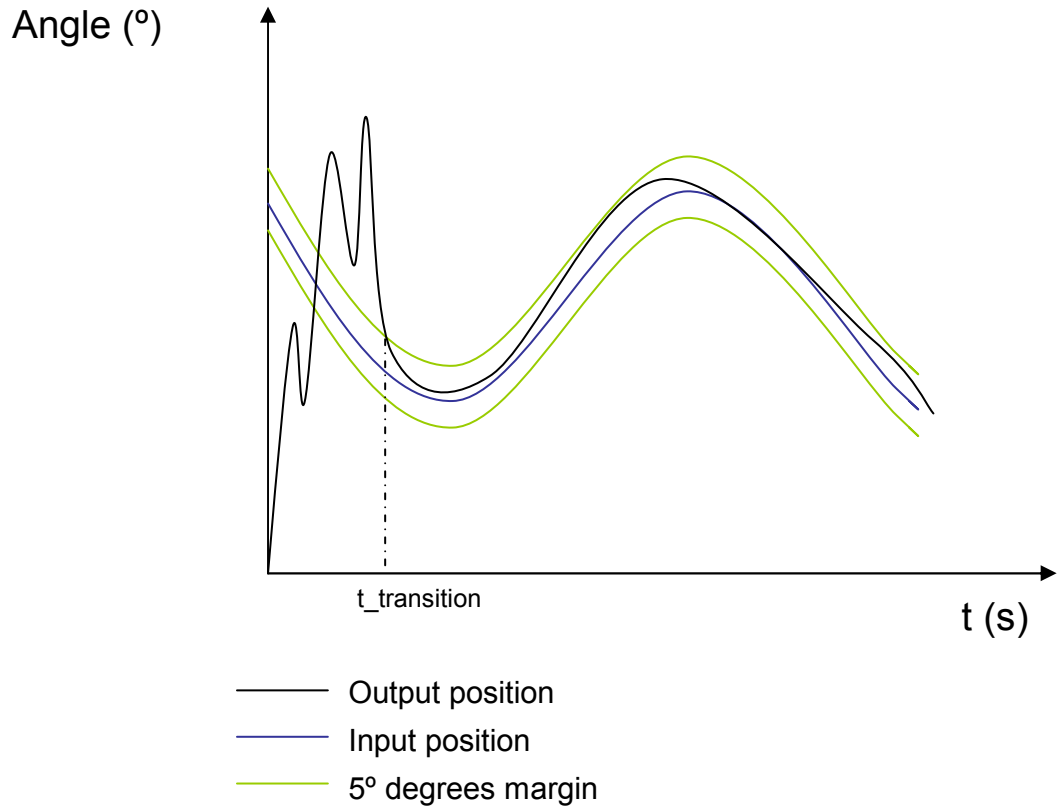

Figure 28 - Detection of transition phase

3.3.2 Scaling procedure

The trajectory used to test the robot and the spacesuit simulator joint cannot be used directly to measure the torque due to the robot's weight (because the output angles are considerably between trials with and without the physical joint brace). The only reliable method to remove the robot's torque from the collected data is to use the output trajectory (in angles) and feed it as an input trajectory to the robot. In this manner, torques are compared at the same angles. However, there is a difference between the input and the output angles in general (Figure 18). Thus, the input angles in the trial without the spacesuit simulator joint had to be scaled appropriately so that the output angles are the same as the trial with the spacesuit simulator joint.

This scale was simply:

$$Scale = \frac{Max\_angle\_with\_joint - Min\_angle\_with\_joint}{Max\_angle\_without\_joint - Min\_angle\_without\_joint}$$

Equation 8

The new input angles for the trial without the brace were found by the following iterative procedure:

$$\begin{cases} \alpha_{input\_without\_brace\_scaled}^{\ 0} = \alpha_{input\_without\_brace\_not\_scaled}^{\ 0} \\ \alpha_{input\_without\_brace\_scaled}^{\ i} = \alpha_{input\_without\_brace\_scaled}^{\ i-1} + \\ scale \times (\alpha_{input\_without\_brace\_not\_scaled}^{\ i} - \alpha_{input\_without\_brace\_not\_scaled}^{\ i-1}) \end{cases}$$

Equation 9

Note: The index 0 corresponds to the transition point

Figure 29 is an example of the result of this scaling procedure:

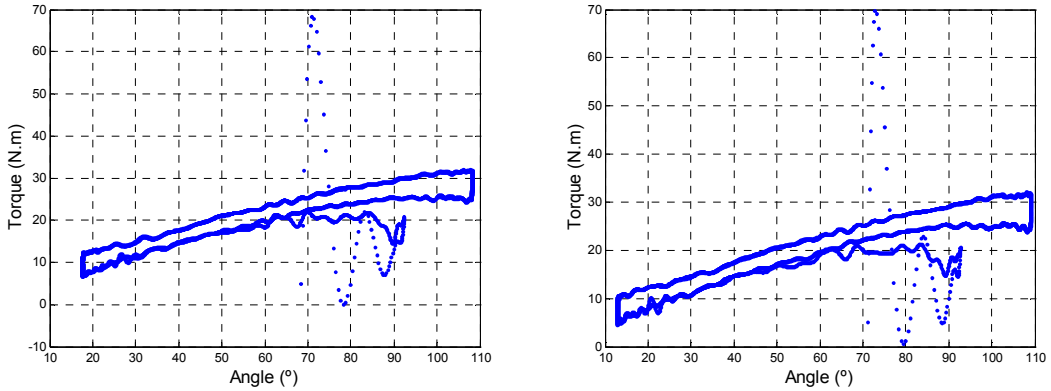

With scaling effect Without scaling effect

Figure 29 - Effect of the scaling process on the trial without the spacesuit simulator joint (difference in the total angle range). This noise found in this picture is due to the fact that the transition phase of the robot was not removed.

After the scaling process, the data is synchronized in both time and angle, i.e. the torque subtraction is done at the same time and at the same angles so that we get coherent results to generate the hysteresis plots.

CHAPTER 4 - Test configuration

Like it was mentioned before, my work was integrated in the first phase of test of the simulator, which corresponded to the study of the knee flexion joint of the space suit simulator.

4.1 Knee joint of the space suit simulator

The knee joint of the space suit simulator would need to be, according to NASA's statement of work, adjustable in terms of:

- Range of maximum angles,
- Friction,
- Stiffness.

Here is the design that implemented the necessary adaptability:

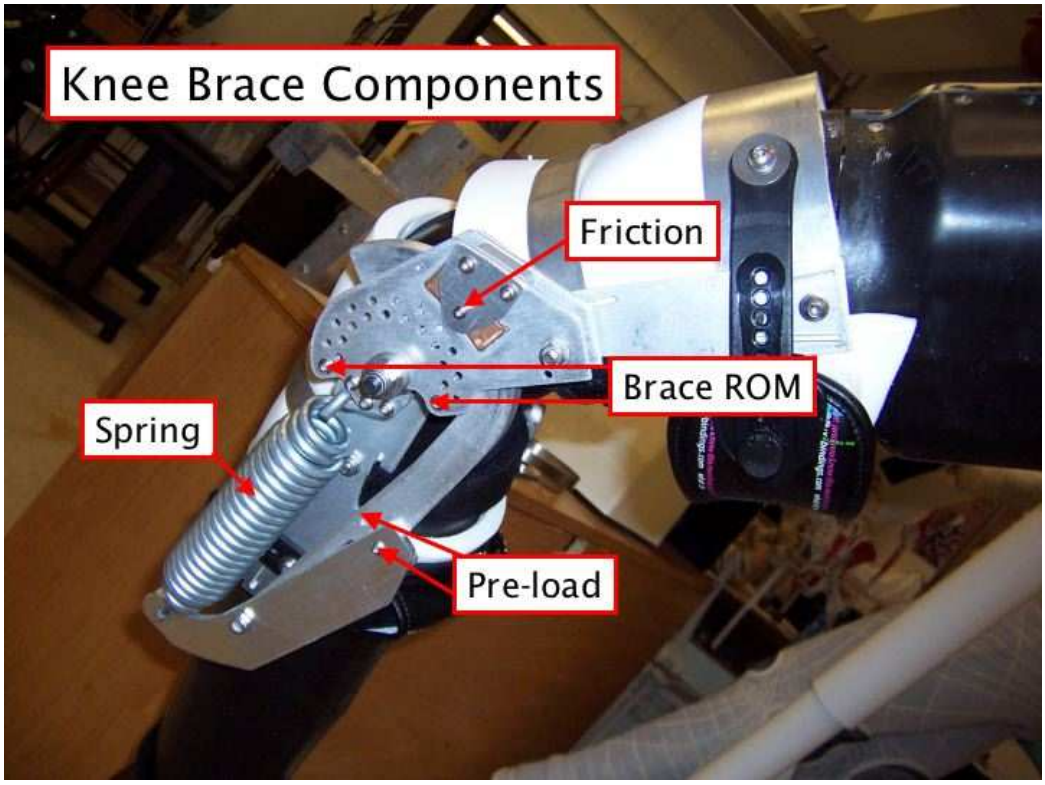

Figure 30 - Knee flexion joint of the space suit simulator

Note: The change of the stiffness of the joint was accomplished by changing the spring at its pre-load.

4.2 Knee joint installation on the robot

After the appropriate brace configuration was set up, the brace was installed on the robot. Initially there were problems with the brace deflecting and sliding on the robot leg, but eventually this was solved by securing the brace to the robot using three modifications: a metal “saddle” extension piece created by ATA, foam pieces inserted between the straps and robot leg, and a hose clamp. Prior to data collection, it was assured that the brace was not shifting on the robot leg. A photo of this setup is shown in Figure 31.

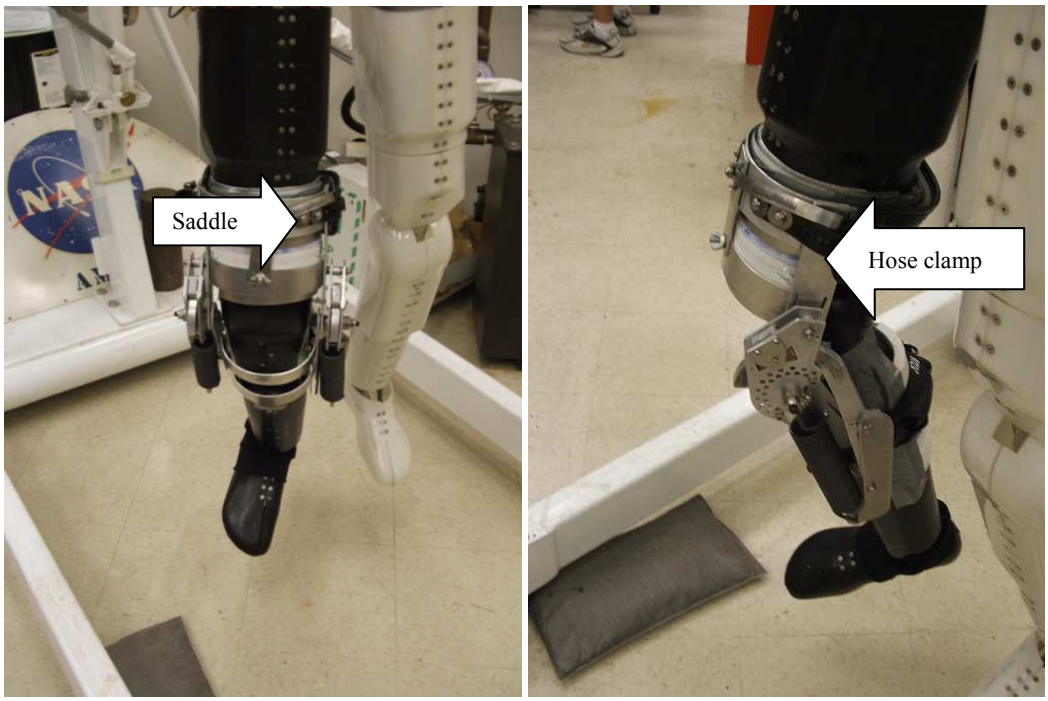

Figure 31 - Brace setup on robot leg with hose clamp, foam, and saddle extension

4.3 Testing procedure

Testing was performed according to configurations specified in the text matrix, located in the experimental protocol (Appendix A). We characterized the effects of adjusting joint speed, range of motion, friction, stiffness, and pre-load conditions on the hysteresis behavior of the joint. Detailed descriptions of the test trajectories used are presented in the protocol, Appendix A. Data collected is presented in angles and torques versus time. Most of the configurations were tested over three trial runs, with the exception of the following configurations: configurations 15-17, where no springs were attached to the brace; and configurations 24-30, where EMU data and human trajectories were used.

4.4 Data Filtering and processing

Collected angle and torque data were Butterworth filtered (10^{th} order filter with a cut-off frequency of 10% of the padding frequency) to remove noise and processed to remove the transition region (the part of the data that corresponded to the robot leg moving into its initialization position).

The complete procedure of the data processing was detailed on Pag.20.

CHAPTER 5 - Results

As stated in the Introduction, the scope the testing prcedure specified in the work plan was as follows:

- Characterize the sensitivity of the joint torque versus angle relationship on joint displacement speed.
- Characterize the hysteresis behavior of the joint.
- Quantify the adjustability of joint range of motion.
- Quantify the adjustability of joint friction.
- Quantify the adjustability of joint stiffness.

Testing results for these five parameters are presented in this section, along with an analysis of brace repeatability over three trials per configuration. Graphs from each individual configuration can be found in Appendix B. Definitions for the parameters varied (speed, joint range of motion, etc.) can be found in the experimental protocol (Appendix A).

The brace was attached in a way that prevented relative motion of the brace on the upper attachment. Since the axis of rotation of the joint was not aligned with the axis of rotation of the robot knee, the joint slid up and down on the lower attachment (back of the calf). The joint was adjusted to cross the zero torque value at an angle of 20°.

All the results are influenced by the robot torque limit (-84.8 Nm, 84.8 Nm). When the torque applied to the robot is greater than this range of values, the robot cannot move past that point. This fact accounts for the differences between the input and the output ranges of motion.

Additionally, all graphs show hysteresis of the joint. This is an artifact of the robot and was characterized earlier[8].

5.1 Sensitivity of the joint torque versus angle relationship to joint displacement speed

Figure 32 shows the difference in the same trajectory at 25°/s (half) speed and 50°/s (full) speed.

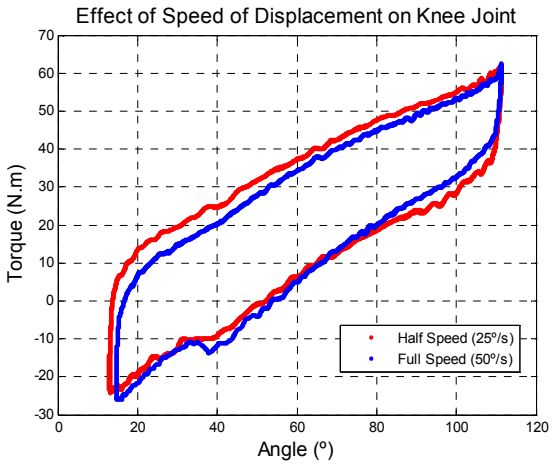

Figure 32 - Effect of speed of displacement on the hysteresis graph of the knee joint

The trajectories run in each trial are shown in Appendix A.
Adjusting trajectory speed has little effect on maximum joint torques. However, in the full speed trial the lower limit of the range of motion occurs sooner, suggesting that in the full speed trial the torque limit is obtained at a smaller range of motion than for the half speed trial.
This discontinuity of the results during the lower part of the trajectory (less than approximately 40º), which is enhanced by the higher speed of the trials, will be seen throughout the experiment and is probably due to instability of the brace for this range within the trajectories.

Although there is only a small difference in terms of the ranges of either angles or torque, in general the area of the graph of the trial run in half speed represents higher torques than the trial run at full speed, suggesting that the energy loss is higher at lower speeds (this effect will be evaluated later in the Energy Loss section of this report, Pag. 33).

5.2 Sensitivity of the joint torque versus angle relationship to the limitation of the joint range of motion

Joint range of motion limits were set by manually setting the position of four screws (Figure 33). Despite the well-calibrated position of these screws in the knee joint, the robot was still able to move beyond these limits because the knee brace axis of rotation does not align with the robot knee axis of rotation. This misalignment, caused by the robot not being perfectly anthropometric, results in relative motion of the lower attachment of the joint against the back calf of the robot, allowing for an increase in the range of motion. For example, when the range was limited to [40º,90º], actual output ranged from [25º,105º].

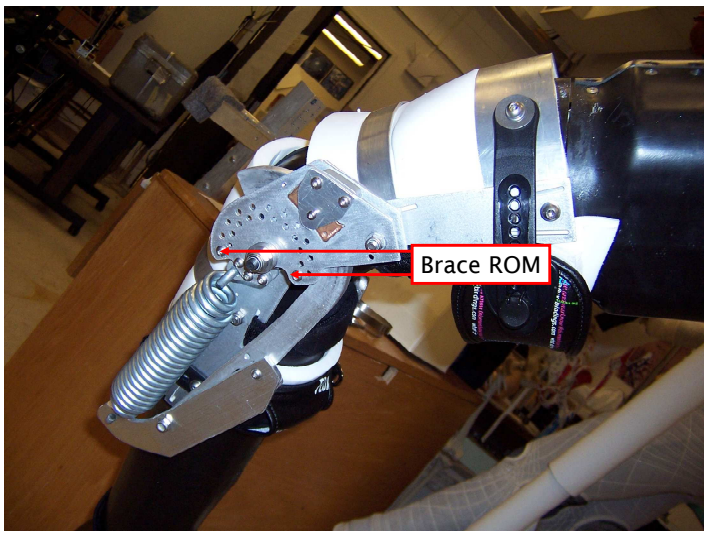

Figure 33 - View of two of the four screws used to change the limits of the range of motion.

Three configurations of the knee joint were tested, one without any limitation of the range of motion [0º,130º], and two smaller ranges ([20º,110º] and [40º,90º]).

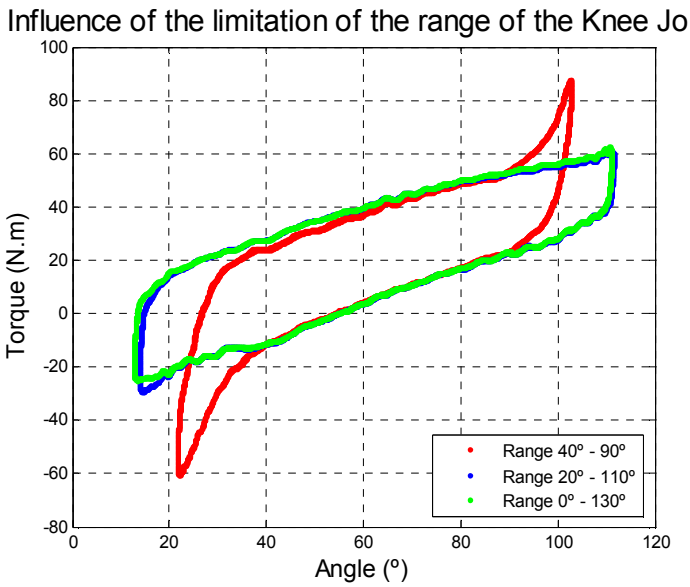

Figure 34 - Effect of the limitation of the range on the hysteresis graph of the knee joint

All results can be found in Appendix B.

The two higher ranges of motion are nearly identical, except for a small difference near the lower limit. The similar behavior of these two cases can be explained by the fact that the robot is unable to reach angles greater than 110º, since the maximum torque limit of the robot joint is reached at this point. The small difference seen at approximately 15° is due to the joint's limitation of the robot's range of motion; the robot was able to move beyond these limits, but in these ranges the robot must "fight" the extra resistance force from the joint.

For the [40°,90°] case, there is a noticeable difference in the behavior of the knee joint. The results begin to diverge at the limits of the range of motion (40º and 90º, lower and upper limits respectively). This extra torque due to the joint is about 40 N∗m for the lower angles and 30 N∗m for the higher angles. The robot reaches the torque limit earlier at higher angles due to the fact that the perpendicular acceleration of gravity contributes to the torque in these positions.

5.3 Sensitivity of the joint torque versus angle relationship to the friction adjustment

Friction was adjusted as described in the experimental protocol (Appendix A). Friction configuration values are also provided in the protocol.

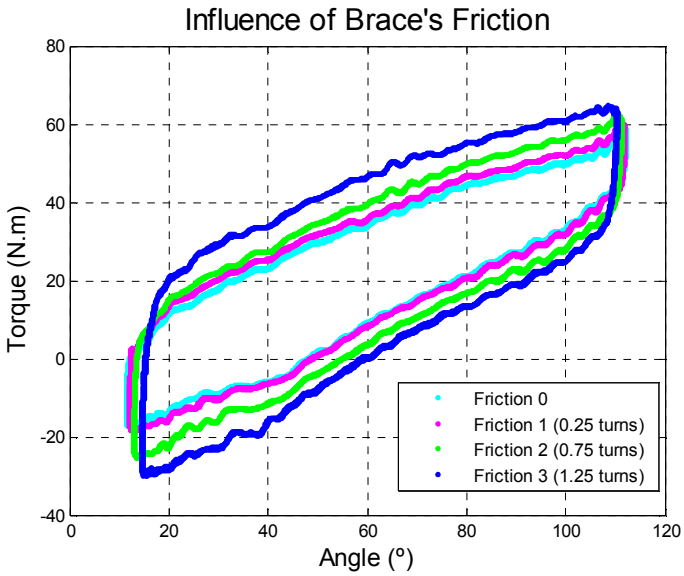

Figure 35 - Effect of friction on the torque vs. angle graph of the knee joint

As expected, the area of the graph visibly increases with the friction, suggesting that the energy loss increases with increasing friction. This effect will be quantified in the Energy Loss section.

Additionally, the range of motion decreases with increasing friction because, as explained above, torque increases at high and low angles (~15° and 110°). The added torque due to the friction of the brake pads will, then, have the net effect of decreasing the range of motion.

Note that even for the smallest friction value (no brake pads) the area of the graph still is greater than Schmidt's EMU data [1] (which can be noticed later on in Figure 38) suggesting that the friction of the brace is still considerably higher than that of the EMU.

5.4 Sensitivity of the joint torque versus angle relationship to the stiffness

Adjustment of joint stiffness was achieved by changing springs. The procedure and the spring values used are described in the experimental protocol (Appendix B). The effect of changing spring stiffness on hysteresis is shown in Figure 36.

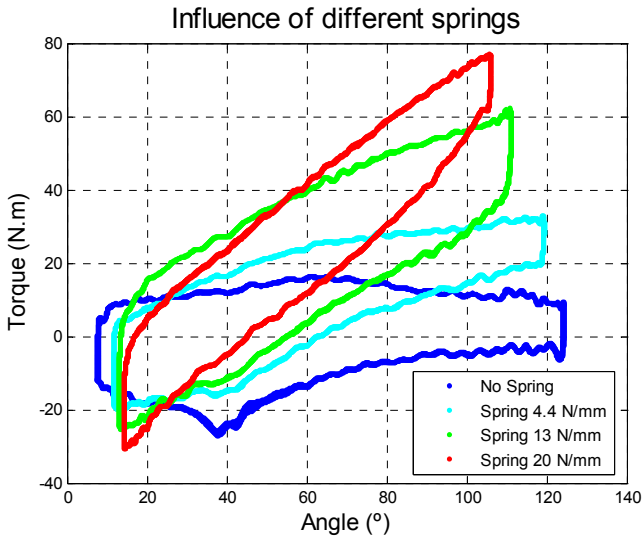

Figure 36 - Effect of stiffness on the hysteresis graph of the knee joint

As expected, increasing the spring stiffness of the knee joint resulted in a change of the slope of the torque vs. angle graph.

Additional properties to note:

- by increasing the spring stiffness, the range of motion of the knee joint decreases because of the torque limitation on the robot, and
- the joint instability that generates the “bump” at around 40º decreases with greater stiffness, suggesting that the force generated by the springs is actually helping with the stability of the knee joint.

The effect of the torque generated by the springs on the overall torque is not linear. This will be detailed on the Model section of this report (Pag. 37).

5.5 Sensitivity of the joint torque versus angle relationship to the Preload

Preload was adjusted as described in the experimental protocol, Appendix A.
Figure 37shows the effect of a center, maximum and a minimum preload.

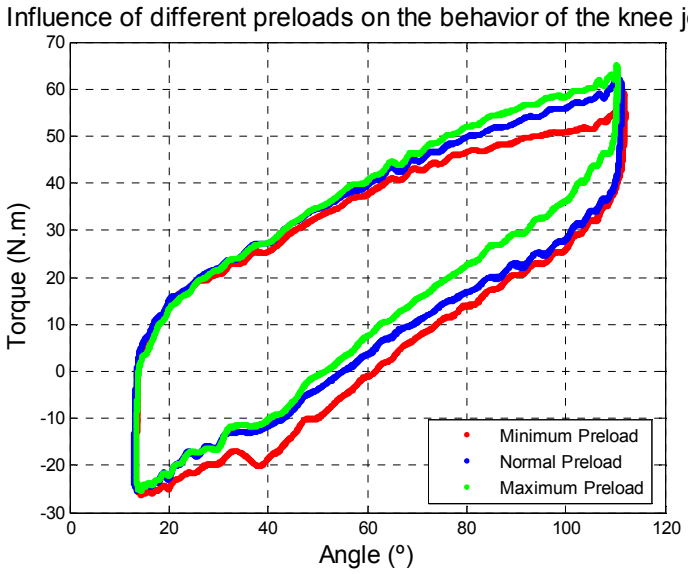

Figure 37 - Effect of preload on the hysteresis graph of the knee joint

Although the effect of a change on the preload of the knee joint is not linear, as is detailed in the Model section of this report, it can be seen that by increasing the preload, the slope of the torque vs. angle graph also increases.

The joint instability that generates a “bump” around 40º decreases with greater preloads.

5.6 EMU comparison

In order to validate the results shown above, and to try to determine the configuration that should be used to mimic EMU conditions, Schmidt’s results [1] were used for comparison.

For this comparison, the file **correcteddata.mat** was used (which concatenates the results from three human trajectories: Subject B,C and E [1]), and the knee joint simulator was set to the EMU conditions:

- Spring Stiffness: 13 N/mm
- Smallest Preload
- Friction: 2

Results for the EMU comparison are shown in Figure 38.

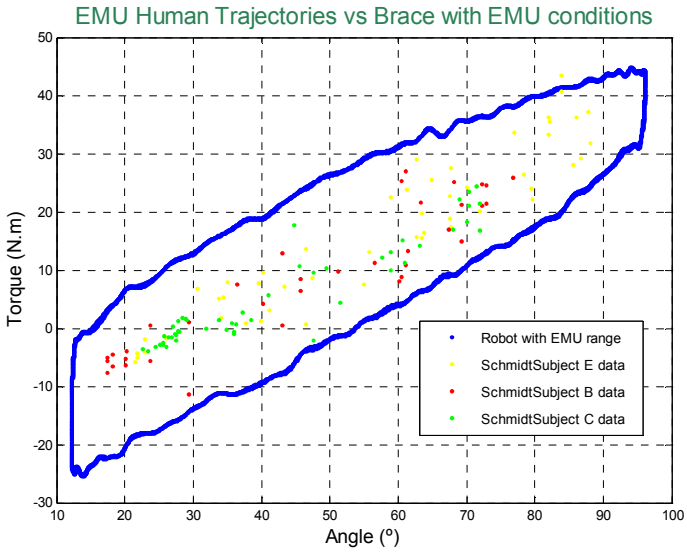

Figure 38 - Comparison between the Knee joint with EMU condition and Schmidt's data[8]

Several additional tests were conducted to compare these results. The same human trajectories run by the different subjects (subject B,C and E) were loaded into the robot, the results can be found in Figure 38.

Although Figure 38 compares human trajectories with a sinusoidal trajectory (blue line), the results obtained with the knee joint simulator seem to fit well with Schmidt's data. Most of the data points obtained by Schmidt fall within the nominal EMU test configuration used for these test runs.

Nevertheless, it is still apparent that the friction (energy loss) on the knee joint is considerably higher for our data than for Schmidt's EMU data (even with the zero friction condition, as noted earlier (Figure 35)). This problem must be addressed.

Some of the differences in the results can also be due to a potential source of error in Schmidt's data analysis. Schmidt removed the torque due to the weight of the robot by synchronizing times rather than angles. In other words, the torques were subtracted at equal times and not at equal angles, which is inappropriate because angles achieved in the trial with the spacesuit were different than those without the spacesuit. In our analysis, we subtracted robot weight based on angle values.

5.7 Energy Loss

In order to characterize the energy loss due to bending the brace in different configurations, a method to calculate this loss had to be developed.

5.7.1 Method to calculate energy loss

Since:

$$E = \int Force * dx \ , \text{also}$$

$$E = \int Torque * d\theta$$

Equation 10

Then, to calculate the energy loss on a cycle of the brace, we need only to identify a cycle of the brace and use numerical integration.

In order to identify a cycle of the brace from a trial containing several cycles, a script was built which did this automatically by determining the number of crossings between the actual data and a linear interpolation of the data:

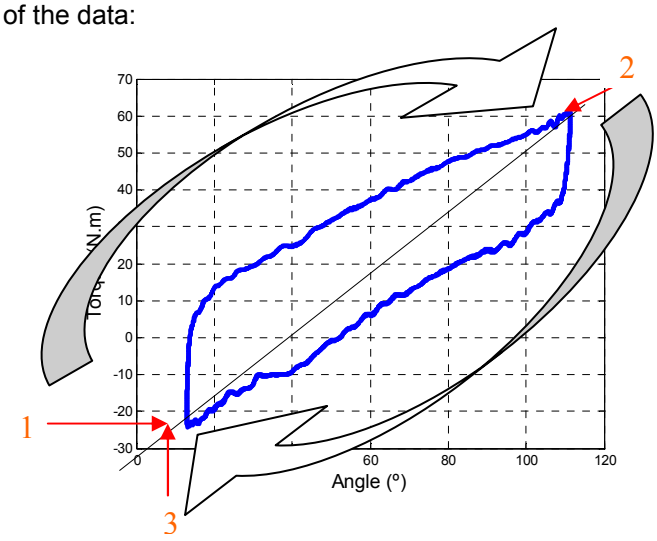

Figure 39 - Identification of one cycle

A cycle was identified by allowing the real data to cross the linear interpolation of the real data two times and defining “how close to stop” from the data was from the third crossing (Figure 39). An example of this identification is shown in Figure 40.

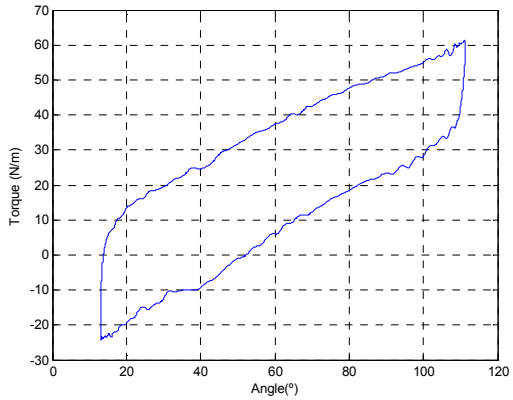

Figure 40 - Example of the identification of a simple cycle of the real data

With this information, the data was integrated numerically:

$$\left\{ \begin{array}{l} x_0 = x_{initial} \\ Integration = \sum_{i=0}^{n-1} \frac{f(x_{i+1}) + f(x_i)}{2} * (x_{i+1} - x_i) \end{array} \right\}$$

Equation 11

Where $x = angle$ in degrees and $f(x) = torque\_at\_angle\_x$ in N.m

Note: Since the values of the angles are in degrees, Equation 10 can be transformed into:

$$E = \int Torque * \frac{\pi}{180} d\theta = Integration * \frac{\pi}{180} \text{ (Joules)}$$

Equation 12

5.7.2 Energy Loss results

- The energy loss increases with the range of motion (trials 12-14, Figure 41):

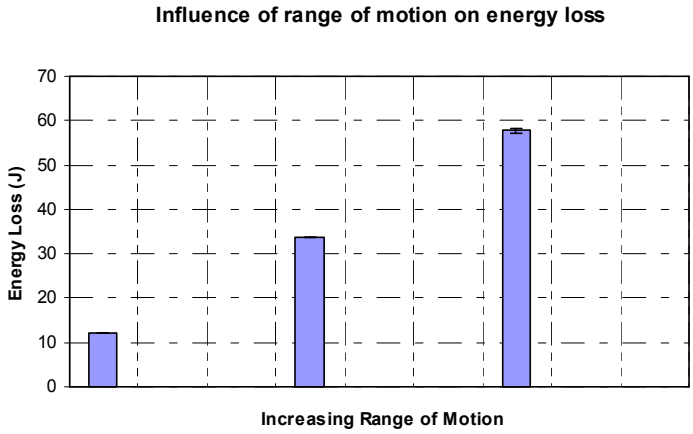

Figure 41 - Influence of range of motion on energy loss

- The energy loss increases when the range of motion is physically limited, rather than inputting a smaller trajectory (by comparing the trials 1-3 with the trials 12-14, Figure 42).

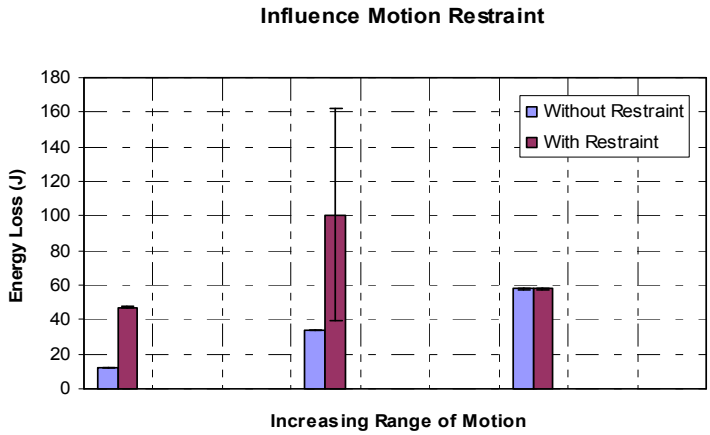

Figure 42 - Influence of motion restraint

- The energy loss increases with increasing friction of the brace (trials 4-7,Figure 43).

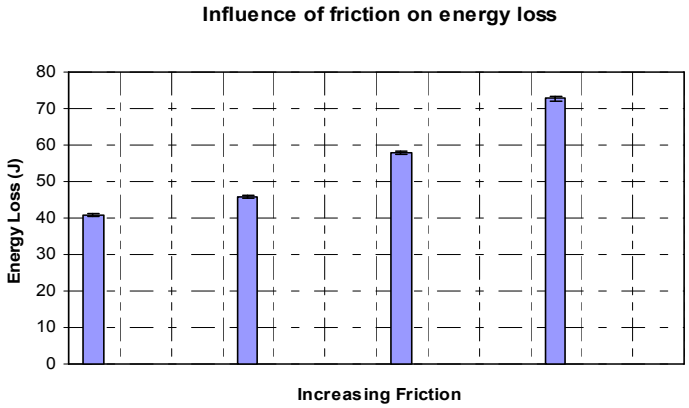

Figure 43 - Influence of friction on energy loss

- The energy loss decreases with the speed of the trajectory (trials 10 and 11,Figure 44).

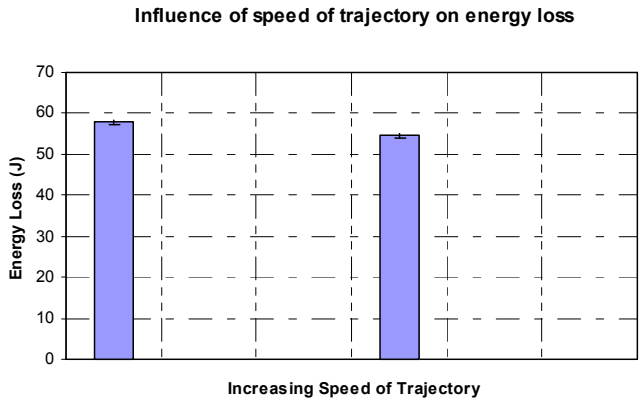

Figure 44 - Influence of speed on energy loss

- The energy loss decreases with greater preloads (trials 8,9 and 3,Figure 45). This was not expected and may be related to the fact that by increasing the preload, the torque limit is

achieved earlier on the robot (at a smaller angle), which reduces the angle range as well as the energy loss.

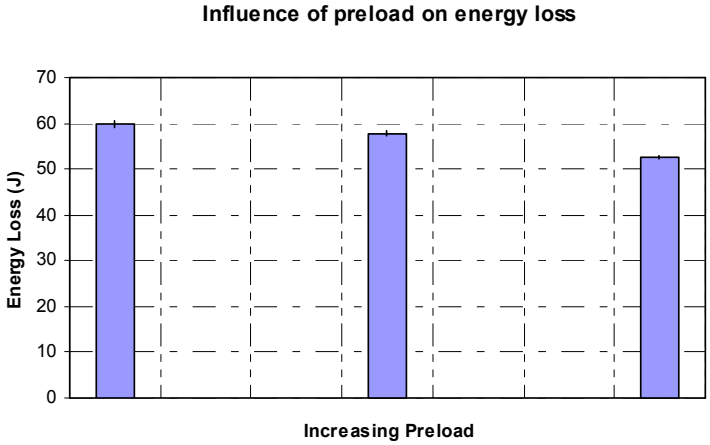

Figure 45 - Influence of preload on energy loss

- There is no clear relationship between the different springs and the energy loss (Figure 47). Theoretically, the energy loss should increase with higher spring constants, but this fact was not verified in testing. The reason for this may be the same as that for the preload effect on energy loss (the torque limit is achieved at smaller angles for higher spring constants, resulting in a smaller range of motion), but further research must be done.

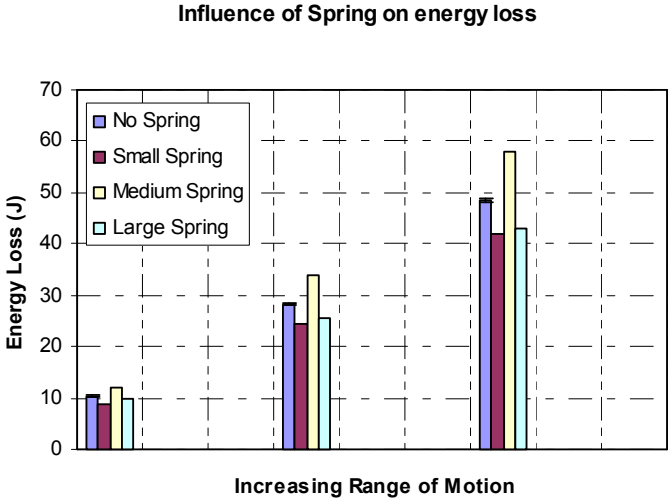

Figure 46 - Influence of different springs on energy loss

CHAPTER 6 - Models

6.1 Physical Model

6.1.1 Methods

We created a physical model to understand the effects of using different springs and preloads. Examining the brace, several parameters can be defined (Figure 47).

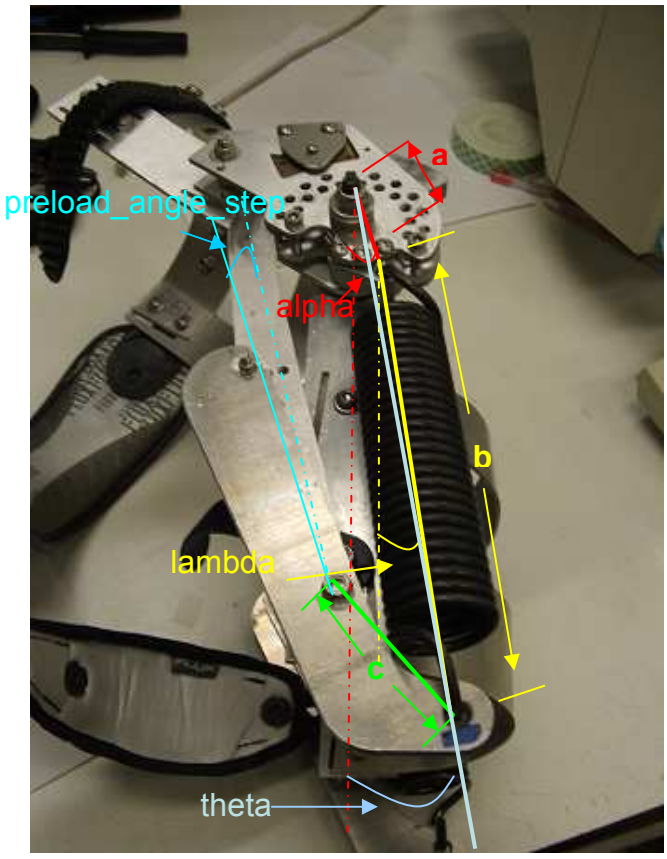

Figure 47 - Parameters of the knee brace

In Figure 47:

- a is the distance between the center of rotation and the upper attachment of the spring,

- b is the non-deflected spring length,

- c is the distance between the rotation point of the piece that regulates the preload and the lower attachment of the spring,

- $alpha$ is the angle between the vertical and the upper attachment of the spring,

- $lambda$ is the angle between the spring alignment and the vertical,

- $theta$ is the angle between the vector formed by the axis of rotation and the lower attachment of the spring and the vertical, and,

- $prelod\_angle\_step$ is the step angle between two screw position (for preload definition)

The values of the fixed variables are given below.

$$a = 0.03m$$
$$b = 0.19m$$
$$c = 0.055m$$
$$alpha = 20^{\circ}$$
$$preload\_angle\_step = 2.73^{\circ}$$

We see that two factors influence the torque generated by the spring:

- When the brace starts bending, spring deflection increases and so the force generated by the spring also increases, and;

- By bending the brace, the projection of the spring force perpendicular to the arm ***a*** increases, which also increases the torque generated by the springs.

The corresponding equation for the torque is

$$T = -2 * F_{spring} * a * (\cos(lambda) * \sin(alpha) + \sin(lambda) * \cos(alpha))$$

Equation 13

And the equation for force due to the spring deflection is

$$F_{spring} = K_{spring} * (Initial\_Load + Deflection)$$

Equation 14

Where K_{Spring} is the spring force constant, $Deflection$ is the increase in the spring's original length, and $Initial\_Load$ is the spring preload.

6.1.2 Spring Deflection

To determine spring deflection as a function of brace bending angle (*theta*), it was necessary to determine the intersection between a circle centered in the joint axis of rotation and a line representing the spring, as shown below in Figure 48.

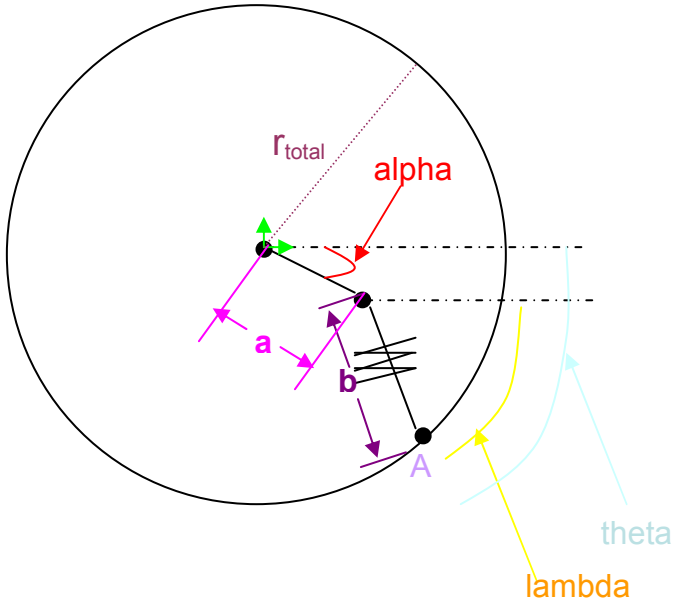

Figure 48 - Scheme to explain physical behavior of the knee brace

Note: The arrows in green represent the origin of the coordinate system, where the *x*-direction is horizontal and the *y*-direction is vertical.

The position of point A can be found using the following formulas:

$$\left\{\begin{matrix} x = r_{total} * \cos(-theta) \\ y = r_{total} * \sin(-theta) \end{matrix}\right\} = \left\{\begin{matrix} x = \sqrt{(a*\cos(alpha)+b)^2 + (b*\sin(alpha))^2} * \cos(theta) \\ y = -\sqrt{(a*\cos(alpha)+b)^2 + (b*\sin(alpha))^2} * \sin(theta) \end{matrix}\right\}$$

Equation 15

The resulting points for $theta \in [0^o, 130^o]$ are shown in Figure 49.

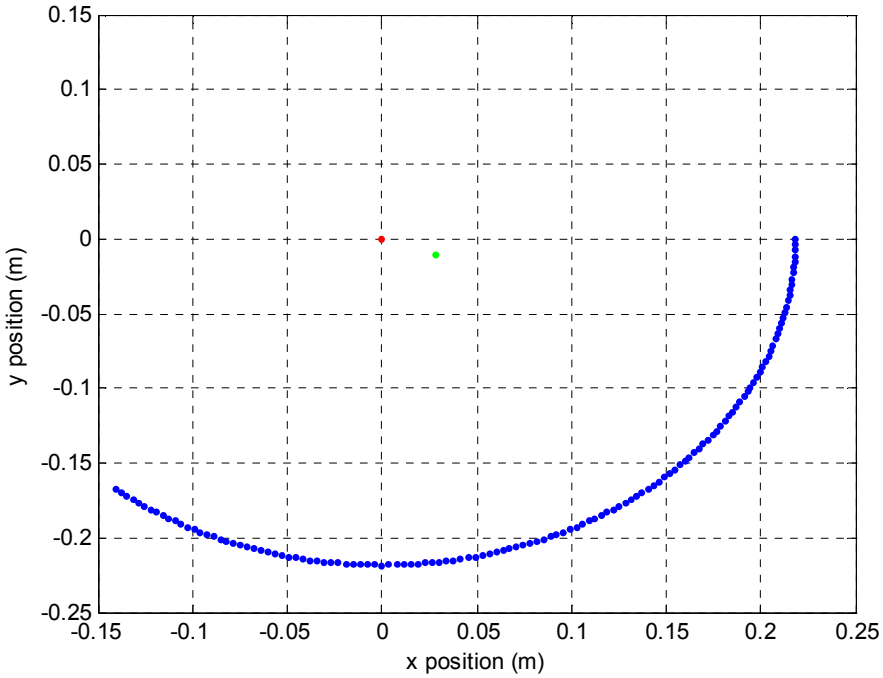

Figure 49 - Evolution of the tip of the spring

Note: The blue points represent the intersection points, the green dot represents the upper attachment of the spring, and the red dot represents the joint's axis of rotation.

The deflection was found by simply calculating the difference between the final and the initial lengths of the spring:

$$deflection = \sqrt{\left(x - a * \cos(alpha)\right)^2 + \left(t + a * \sin(alpha)\right)^2} - b$$

Equation 16

6.1.3 Spring's force

To calculate spring force, the $Initial\_Load$ of the spring had to be determined.

This was defined as:

$$Initial\_Load = Max\_\mathrm{Pr}eload - \left(c * preload\_angle\_step * \frac{\pi}{180}\right) * n$$

Equation 17

Where *Max_Preload* represents the maximum preload of the spring (with the screw in the last position for preload regulation on the brace) and n represents the position of the screw to generate additional preload ($n \in \{1,2,3,4,5\}$).

Note: $n = 0$ at the maximum preload position and increases towards the lower preload positions.

The force of the spring as a function of the angle of the brace (*theta*), for the medium spring ($K_{Spring} = 13N/mm$) set at a medium preload ($n = 3$), is given in Figure 50.

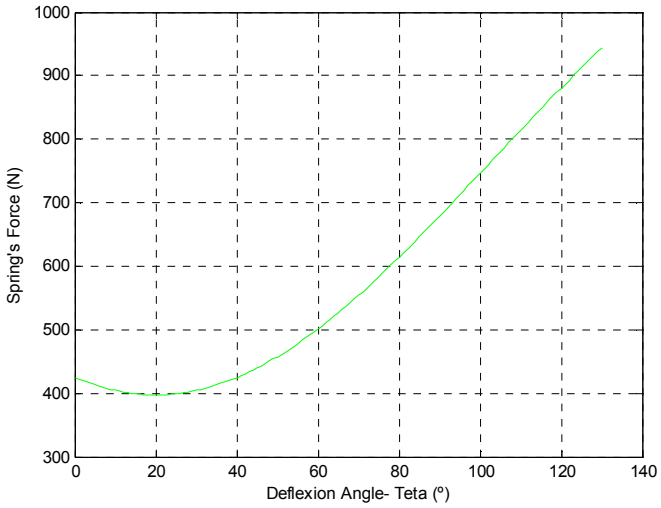

Figure 50 - Evolution of the force generated by the spring with the angle of the brace

Note: The value of the force was found using Equation 14.

As expected, the force generated by the spring is minimum when the angle of the brace is $alpha$ = 20º, a fact that can be easily understood from by Figure 48.

6.1.4 Torque generated by the springs

To calculate the torque generated by the springs, $lambda$ had to be found with the following equation:

$$lambda = a\tan\left(\frac{y + a * \sin(alpha)}{x - a * \cos(alpha)}\right)$$

Equation 18

From Equation 13, the torque generated by the springs as a function of the angle of the brace (*theta*) using a medium spring ($K_{Spring} = 13N/mm$) and a medium preload ($n = 3$) is shown in Figure 51.

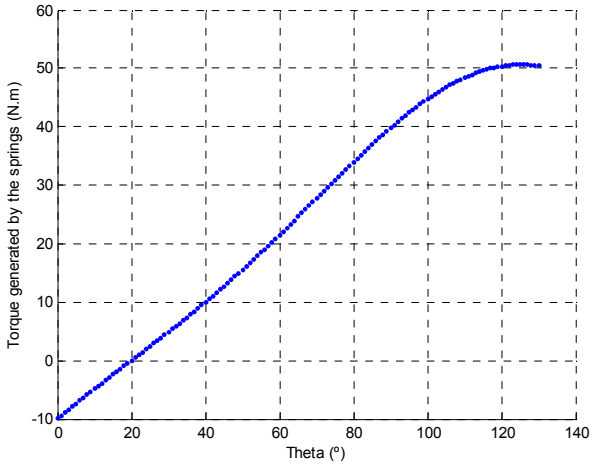

Figure 51 - Torque generated by the springs vs. Deflection Angle

6.1.5 Results of the physical model

We compared the model's results against the brace's actual behavior. Since this model does not account for the hysteresis behavior of the brace, all that can be compared is the general trend of the hysteresis data found during testing.

This model allows the analysis of the effect of a change on the preload position of the brace or the effect of a new spring, seen in Figure 52.

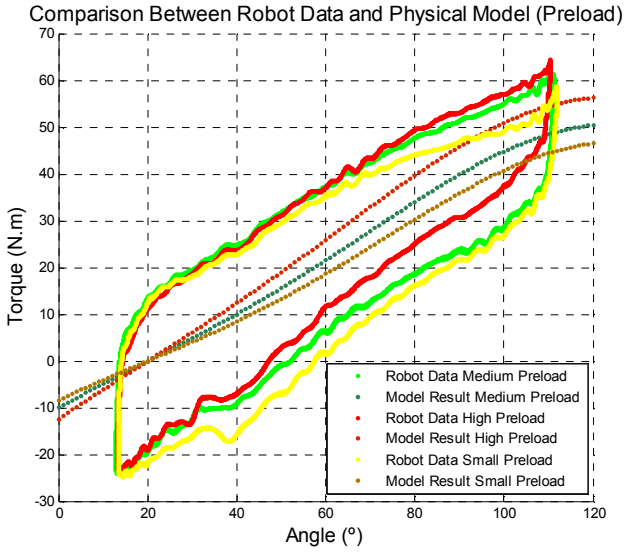

Figure 52 - Effect of a preload change (comparison with real data)

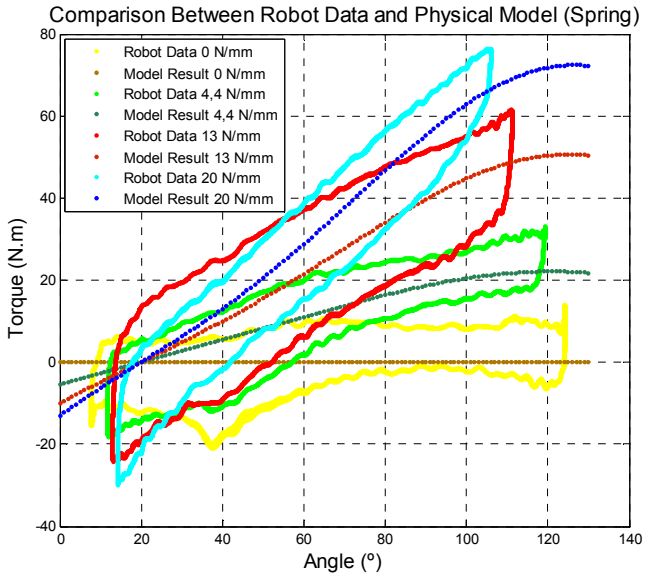

Figure 53 - Effect of a spring change (comparison with real data)

6.1.6 Final comments on the physical model

Although this model does not account for the hysteresis behavior of the brace, the general shape of the torque-angle curve generated by the model fits well with the actual torque data collected during our robot testing.

Differences between the model and experimental results can also be seen because the model does not take into consideration the change of the zero torque crossing point with the change in the springs of the brace, or the torque generated by the braking system, which is designed to add friction to the brace.

6.2 Mathematical Model

Since the physical model could not explain the hysteretic effect of the joint, a new model, this time a mathematical one, was developed.
It is first of all necessary to have an idea of the hysteretic reason of the phenomenon.

6.2.1 Hysteretic behavior

The hysteresis behavior is common amongst a lot of physical models. We can find this effect in structural elements like concrete or steel. [1]
A simplified conceptual model of the hysteretic behavior is shown on the next figure:

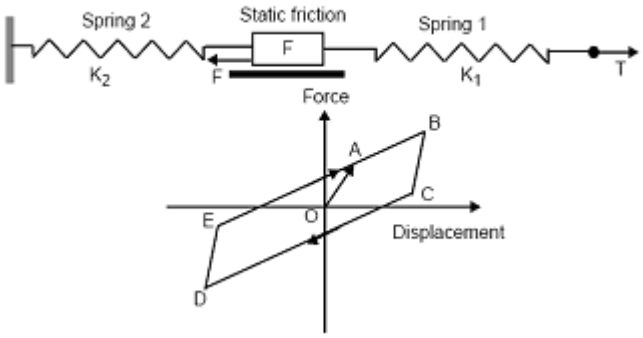

Figure 54 - Simplified model of hysteretic behavior[7]

The model consists of two springs in series surrounding a static friction element. When an extensional force is applied at spring 1, spring 1 initially extends. This corresponds to a shear deformation of the fabric, without the yarns sliding over each other, and the force-displacement curve follows line OA of Figure 54.
When the tension in spring 1 exceeds the static friction force, *F*, the static friction element slides and stretches spring 2. Sliding of the static friction element corresponds to yarns in the fabric sliding over each other. This phase corresponds to line AB on the force displacement plot. When the direction of the force at spring 1 is reversed, initially, only spring 1 will compress, corresponding to elastic recovery of the fabric without yarn shifting, on line BC of the force-displacement plot of Figure 54. As in the extension case, when the compressive force in spring 1 exceeds the static friction force F, the friction element slides, compressing spring 2 along line CD. Finally, if the extensional force is applied again at spring 1, spring 1 will initially extend (line DE) and when the tension in spring 1 exceeds the static friction force F, the frictional element will slide and extend spring 2, along line EA of the force-displacement plot, completing the hysteresis loop.

6.2.2 Bouc-Wen model

There are many mathematical models to effectively describe a hysteretic behavior. One of most popular is the class of the hysteretic models Bouc-Wen, which were suggested by Bouc in 1967 and generalized later by Wen in 1976.
The model has the advantage of being easy to implement by means of computer, because only one auxiliary nonlinear equation is necessary to describe the hysteresis.
The model is also flexible because it accounts for various characteristics of the hysteretic behavior such as for example the degradation of rigidity.
For a structural element ruled by a Bouc-Wen hysteretic model, the resisting force can be defined in the following way [1]:

$$f_s(x,\dot{x},z) = \alpha K_0 x + (1-\alpha) K_o z$$

Equation 19

Where *x* represents position, $\dot{x}$ =*dx*/*dt* is the speed of displacement, α is the coefficient that represents the elastic behavior proportion (if α = 1, the resisting force is fully elastic), K_0 is the initial stiffnessest and *z* is an auxiliary variable that represents the inelastic behavior.

The evolution on z follows the following ordinary differential equation:

$$\dot{z} = \dot{x}\left[A - |z|^n \Psi(x,\dot{x},z) \right]$$

Equation 20

Where $\dot{z}$ =*dz*/*dt* is the virtual speed of displacement of *z*; *A* and *n* are parameters that control the scale and stiffness of the different hysteresis loops; $\Psi(x,\dot{x},z)$ is a non linear function of *x*, $\dot{x}$ and *z* that the controls the shape of the hysteresis loops.

The $\Psi(x,\dot{x},z)$ functions of the original Bouc-Wen model (Wen 1976) and the Wang the Wen model (1998) are:

$$\Psi(x,\dot{x},z)_{Bouc-wen} = \gamma + \beta\,\mathrm{sgn}(\dot{x}\,z)$$
$$\Psi(x,\dot{x},z)_{Wang-wen} = \gamma + \beta\,\mathrm{sgn}(\dot{x}\,z) + \phi\left[\mathrm{sgn}(\dot{x}) + \mathrm{sgn}(z) \right]$$

Equation 21

6.2.3 Bouc-Wen model application to our results

As it can be seen (for example in Appendix B), the obtained hysteresis loops are often affected by more than only the signs of and $\dot{x}$ and *z*. They are also influenced by the sign of displacement *x*, because the behavior hysteretic of the knee joint is different if it is being stretched of compressed [9].

The existing Bouc-Wen models do not include *x* in the function $\Psi(x,\dot{x},z)$ (Equation 21), and this is why they cannot adapt to asymmetrical hysteretic behaviors.

To sort out this limitation, a new definition of the $\Psi(x,\dot{x},z)$ functions was created:

$$\Psi(x,\dot{x},z) = \beta_1 \operatorname{sgn}(\dot{x}\,z) + \beta_2 \operatorname{sgn}(\dot{x}\,x) + \beta_3 \operatorname{sgn}(xz) + \beta_4 \operatorname{sgn}(\dot{x}) + \beta_5 \operatorname{sgn}(z) + \beta_6 \operatorname{sgn}(x)$$

Equation 22

This new definition as six degrees of freedom, thereby it can control the hysteresis phase in six different regions.
Figure 55 shows, in a hysteresis cycle, the different phases of this new definition of the model determined by the different combinations of *x*, $\dot{x}$ and *z*.

Table 4 gives the corresponding values of the $\Psi(x,\dot{x},z)$ function [9]:

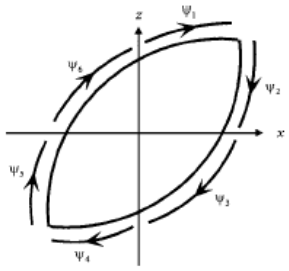

Phase	x	$\dot{x}$	z	$\psi(x,\dot{x},z)$
1	+	+	+	$\psi_1=\beta_1+\beta_2+\beta_3+\beta_4+\beta_5+\beta_6$
2	+	−	+	$\psi_2=-\beta_1-\beta_2+\beta_3-\beta_4+\beta_5+\beta_6$
3	+	−	−	$\psi_3=\beta_1-\beta_2-\beta_3-\beta_4-\beta_5+\beta_6$
4	−	−	−	$\psi_4=\beta_1+\beta_2+\beta_3-\beta_4-\beta_5-\beta_6$
5	−	+	−	$\psi_5=-\beta_1-\beta_2+\beta_3+\beta_4-\beta_5-\beta_6$
6	−	+	+	$\psi_6=\beta_1-\beta_2-\beta_3+\beta_4+\beta_5-\beta_6$

Figure 55 - Evolution of shape control function ($\Psi(x,\dot{x},z)$) in a hysteresis cycle

Table 4 - Corresponding values of the $\Psi(x,\dot{x},z)$ function

Note: Since the hysteretic behavior graphs of the knee joint (Appendix B) were not center at the origin (there were no negative angles), all the values were subtracted of the trial average, so that the graph is center on the point (0, 0).

Using the finite differences method (first order) applied to Equation 20 the following iterative method was developed:

$$
\begin{cases}
z_0 = Initial\_Torque \\
x_0 = Initial\_Angle \\
z_{i+1} = (x_{i+1} - x_i)\left[A - |z|^n \Psi_i(x, \dot{x}, z) \right] + z_i \\
\Psi_i(x, \dot{x}, z) = \beta_1 \operatorname{sgn}[(x_{i+1} - x_i) z_i] + \beta_2 \operatorname{sgn}[(x_{i+1} - x_i) x_i] + \beta_3 \operatorname{sgn}[x_i z_i] \\
\qquad\qquad + \beta_4 \operatorname{sgn}[x_{i+1} - x_i] + \beta_5 \operatorname{sgn}[z_i] + \beta_6 \operatorname{sgn}[x_i]
\end{cases}
$$

Equation 23

Where *x* is the joint position angle and *z* is the corresponding torque.

Developing Equation 22 and using the naming convention on Table 4 we can define the matrix shown on 'Equation 24 that can be inversed to arrive at the matrix on Equation 25.

$$
\begin{bmatrix} \Psi_1 \\ \Psi_2 \\ \Psi_3 \\ \Psi_4 \\ \Psi_5 \\ \Psi_6 \end{bmatrix} = \begin{bmatrix} 1 & 1 & 1 & 1 & 1 & 1 \\ -1 & -1 & 1 & -1 & 1 & 1 \\ 1 & -1 & -1 & -1 & -1 & 1 \\ 1 & 1 & 1 & -1 & -1 & -1 \\ -1 & -1 & 1 & 1 & -1 & -1 \\ 1 & -1 & -1 & 1 & 1 & -1 \end{bmatrix} \begin{bmatrix} \beta_1 \\ \beta_2 \\ \beta_3 \\ \beta_4 \\ \beta_5 \\ \beta_6 \end{bmatrix}
$$

Equation 24

$$
\begin{bmatrix} \beta_1 \\ \beta_2 \\ \beta_3 \\ \beta_4 \\ \beta_5 \\ \beta_6 \end{bmatrix} = \frac{1}{4} \begin{bmatrix} 1 & 0 & 1 & 1 & 0 & 1 \\ 0 & -1 & -1 & 0 & -1 & -1 \\ 1 & 1 & 0 & 1 & 1 & 0 \\ 1 & -1 & 0 & -1 & 1 & 0 \\ 0 & 1 & -1 & 0 & -1 & 1 \\ 1 & 0 & 1 & -1 & 0 & -1 \end{bmatrix} \begin{bmatrix} \Psi_1 \\ \Psi_2 \\ \Psi_3 \\ \Psi_4 \\ \Psi_5 \\ \Psi_6 \end{bmatrix}
$$

Equation 25

With the tools described before, a procedure was developed to arrive at the hysteretic model of each configuration in which the joint was tested.

The next figure describes that procedure:

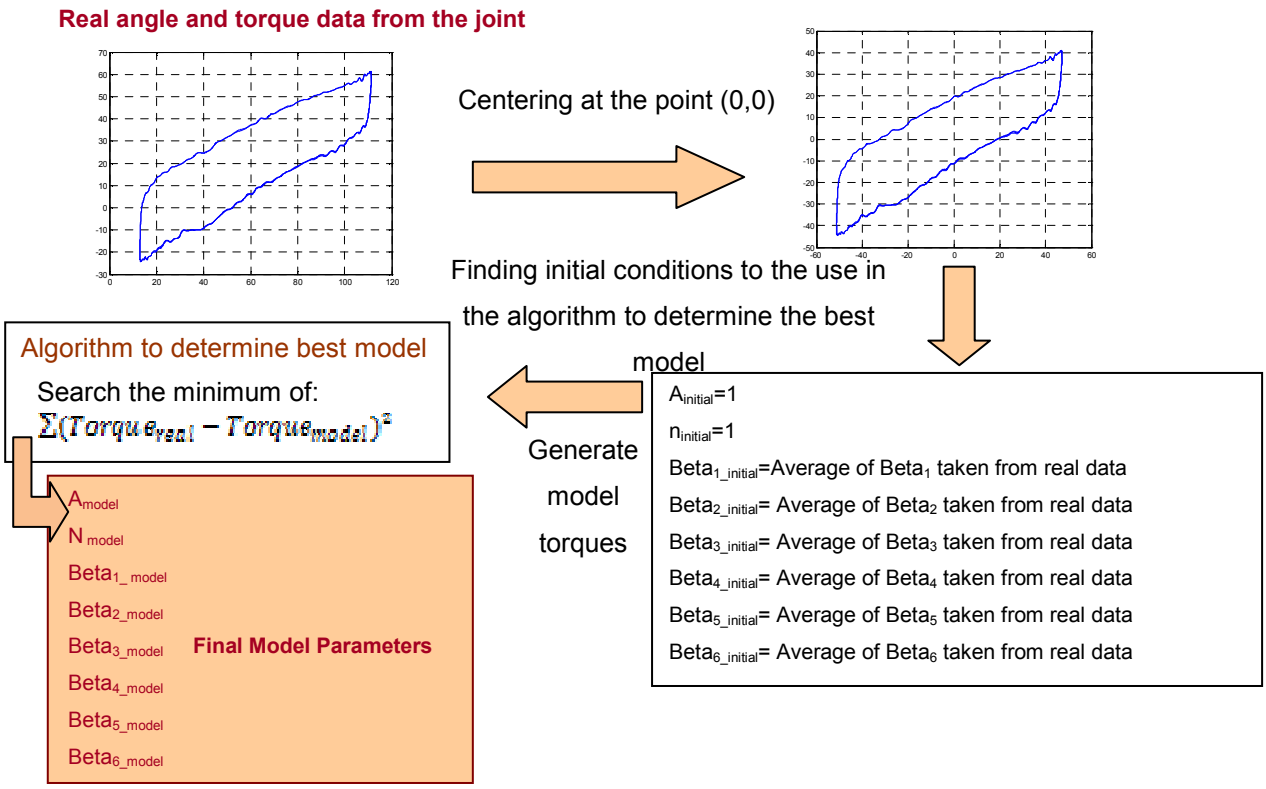

Figure 56 - Procedure to determine mathematical model

Where the centering at the point (0,0) procedure of the data was described before; the finding of the initial conditions was made by averaging the real data (by using the Equation 22 and Equation 25); the generation of the model torques was done using Equation 23 and; the algorithm to determine the best model was the minimum square difference between the real torques (found by testing) and the torques predicted by the model.

6.2.4 Results of the mathematical model

After obtaining the mathematical model for each joint configuration, it was possible to compare the results between the real torques (found by testing) and the torques predicted by the model. The next figures show an example of those results using the knee joint at a configuration with K_{spring}=13N/mm and a braking torque of 3,75N.m:

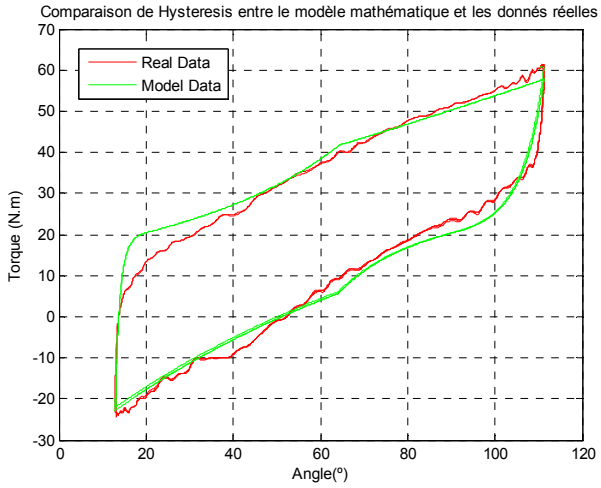

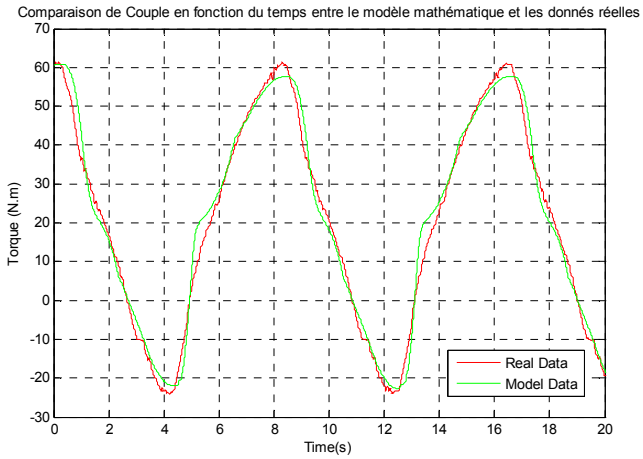

Figure 57 - Hysteretic behavior comparison between the mathematical model results (A=0,2823 ;n=1,2065;beta1=0,013;beta2=0,145;beta3=-0,1359;beta4=-0,0879;beta5=0,0935; beta6=-0,0036) and real data

Figure 58 - Torque comparison between the mathematical model results (A=0,2823 ;n=1,2065;beta1=0,013;beta2=0,145;beta3=-0,1359;beta4=-0,0879;beta5=0,0935; beta6=-0,0036) and real data

6.2.5 Final comments on the mathematical model

After the analysis of the comparison of the results predicted by the mathematical model and the torque obtained by testing the robot it was easily noticed that this type of model depends a lot on the initial conditions (i.e. the divergence of the results is intrinsically related to the values of A and N given for the initial iteration).
But, after a suitable treatment of the results, the model was a lot closer to real data.
This type of model can be used in an immediate future to characterize all the joints of the simulator and therefore all the existing and future spacesuits.

CHAPTER 7 - Conclusion

This thesis described the beginning of the development of a space suit simulator which intends to simulate all current and future spacesuits the simulator.
This simulator will allow a reduction of the planning procedures costs, a simplification of the astronauts' training and a better study of the influence of the various parameters of a spacesuit on the behavior of the astronaut.
Tools were created to the use of an anthropomorphic robot, to measure the behavior of the first joint of the simulator, the knee joint.
The analysis of the results was detailed, namely the subtraction of torque due to the robot itself, data filtering and scaling, to arrive at results which allowed the characterization of this joint and the simulation of the current American spacesuit (EMU) configuration.

Physical and mathematical models allowed a validation of the results. The mathematical model used an innovative procedure that can also be applied to other systems with hysteretic behaviors.
The results of this study will allow a better prediction of the necessary torques to bend each joint of the simulator and, as the simulator will allow the simulation of all current and future spacesuits, the characteristics of each spacesuit can also be evaluated.
The results of the models will, in the future, allow a better planning of the extravehicular activities (EVA) as well as a better definition of the astronaut's work envelope(i.e. range of joint positions where the astronaut feels more comfortable working at).

Bibliography

[1] Changai, R. et Lining, S., *Hysteresis and creep compensation for piezoelectric actuator in open-loop operation*. Robot research Institute, Harbin Institute of Technology, China, March 2005.

[2] Frazer, A.L., B.M. Pitts, P.B. Schmidt, E. Hodgson, and D.J. Newman, *Quantifying Astronaut Tasks: Robotic Technology and Future Space Suit Design*. Abstract, Second Biennial Space Human Factors Workshop, Houston, TX, January 2002.

[3] Frazer, A.L., B.M. Pitts, P.B. Schmidt, J.A. Hoffman, and D.J. Newman, *Astronaut Performance: Implications for Future Spacesuit Design*. 53rd International Astronautical Congress, Paper No. IAC-02-6.5.03, Houston, TX, October 2002.

[4] Frazer, A.L., *Modeling human-spacesuit interactions.* Department of Aeronautics and Astronautics, MIT S.M.: 2003.

[5] Newman, D.J., P.B. Schmidt, E. Hodgson, *A Model of Space Suit Joint Mobility with Applications to EVA Operations*. NASA Bioastronautics Inverstigators' Workshop, Galveston, TX, January 2001.

[6] Newman, D.J., P.B. Schmidt, D.B. Rahn, D. Metaxas, and N. Badler, *Modeling the Extravehicular Mobility Unit (EMU) Space Suit: Physiological Implications for Extravehicular Activity (EVA).* AIAA and SAE International Conference on Environmental Systems (ICES 2000), Toulouse, France, July 2000.

[7] Schmidt, P.B., *An investigation of space suit mobility with applications to EVA operations.* Department of Aeronautics and Astronautics, MIT PhD: 2001.

[8] Schmidt, P.B., D.J. Newman, et E. Hodgson, *Modeling Space Suit Mobility: Applications to Design and Operations*. AIAA and SAE International Conference on Environmental Systems (ICES 2001), Orlando, FL, July 2001.

[9] Song, J. et Kiureghian, A.D., *Generalized Bouc-Wen model for highly asymmetric hysteresis*. Journal of Engineering Mechanics-ASCE. 132 (6), pp. 610-618., California, 2006.

Appendix A: Experimental protocol and test matrix

The test matrix showing the parameters to be varied for the various runs is shown below in Table 5. Test trajectories for the runs are shown in Table 6.

Order # (KEY)	Test Run #	Condition being tested	Profile	ROM Brace	ROM Robot	Friction	Stiffness	Speed	Pre-load
1	5	Range of motion of the brace	Sinusoid	R1	Rr3	2	K2	Full	Center
2	6		Sinusoid	R2	Rr3	2	K2	Full	Center
3	7		Sinusoid	R3	Rr3	2	K2	Full	Center
4	8	Friction	Sinusoid	R3	Rr3	0	K2	Full	Center
5	9		Sinusoid	R3	Rr3	1	K2	Full	Center
6	10		Sinusoid	R3	Rr3	2	K2	Full	Center
7	11		Sinusoid	R3	Rr3	3	K2	Full	Center
8	3	Spring pre-load	Sinusoid	R3	Rr3	2	K2	Full	First
9	4		Sinusoid	R3	Rr3	2	K2	Full	Last
10	1	Speed	Sinusoid	R3	Rr3	2	K2	Full	Center
11	2		Sinusoid	R3	Rr3	2	K2	Half	Center
12	18	ROM with medium spring	Sinusoid	R1	Rr1	2	K2	Full	Center
13	19		Sinusoid	R2	Rr2	2	K2	Full	Center
14	20		Sinusoid	R3	Rr3	2	K2	Full	Center
15	12	ROM with no springs	Sinusoid	R1	Rr1	2	K0	Full	Center
16	13		Sinusoid	R2	Rr2	2	K0	Full	Center
17	14		Sinusoid	R3	Rr3	2	K0	Full	Center
18	15	ROM with small spring	Sinusoid	R1	Rr1	2	K1	Full	Center
19	16		Sinusoid	R2	Rr2	2	K1	Full	Center
20	17		Sinusoid	R3	Rr3	2	K1	Full	Center
21	21	ROM with largest spring	Sinusoid	R1	Rr1	2	K3	Full	Center
22	22		Sinusoid	R2	Rr2	2	K3	Full	Center
23	23		Sinusoid	R3	Rr3	2	K3	Full	Center
24	24	Direct EMU comparison	Human	R-E	Subj. B	EMU	K-EMU	Full	EMU
25	25		Human	R-E	Subj. C	EMU	K-EMU	Full	EMU
26	26		Human	R-E	Subj. E	EMU	K-EMU	Full	EMU
27	27		Sinusoid	R-E	Rr-E	EMU	K-EMU	Full	EMU
28	28		Sinusoid	R-E	Rr-E	EMU	K-EMU	Half	EMU

Table 5 - Test matrix describing each trial of the robot

Note: Color means identifies the parameter that varies for each condition being tested

Order # (KEY)	Test Run #	Condition being tested	Profile	ROM Robot	Speed	Trajectory	Data File
1	5	Range of motion of the brace	Sinusoid	Rr3	Full	65+65*sin(2π/8.17 t)	kf1raw#pro_filtered.mat
2	6		Sinusoid	Rr3	Full	65+65*sin(2π/8.17 t)	kf2raw#pro_filtered.mat
3	7		Sinusoid	Rr3	Full	65+65*sin(2π/8.17 t)	kf3raw#pro_filtered.mat
4	8	Friction	Sinusoid	Rr3	Full	65+65*sin(2π/8.17 t)	kf4raw#pro_filtered.mat
5	9		Sinusoid	Rr3	Full	65+65*sin(2π/8.17 t)	kf5raw#pro_filtered.mat
6	10		Sinusoid	Rr3	Full	65+65*sin(2π/8.17 t)	kf6raw#pro_filtered.mat
7	11		Sinusoid	Rr3	Full	65+65*sin(2π/8.17 t)	kf7raw#pro_filtered.mat
8	3	Spring pre-load	Sinusoid	Rr3	Full	65+65*sin(2π/8.17 t)	kf8raw#pro_filtered.mat
9	4		Sinusoid	Rr3	Full	65+65*sin(2π/8.17 t)	kf9raw#pro_filtered.mat
10	1	Speed	Sinusoid	Rr3	Full	65+65*sin(2π/8.17 t)	kf10raw#pro_filtered.mat
11	2		Sinusoid	Rr3	Half	65+65*sin(2π/16.34 t)	kf11raw#pro_filtered.mat
12	18	ROM with medium spring	Sinusoid	Rr1	Full	25+25*sin(2π/3.14 t)	kf12raw#pro_filtered.mat
13	19		Sinusoid	Rr2	Full	45+45*sin(2π/5.65 t)	kf13raw#pro_filtered.mat
14	20		Sinusoid	Rr3	Full	65+65*sin(2π/8.17 t)	kf14raw#pro_filtered.mat
15	12	ROM with no springs	Sinusoid	Rr1	Full	25+25*sin(2π/3.14 t)	kf15raw#pro_filtered.mat
16	13		Sinusoid	Rr2	Full	45+45*sin(2π/5.65 t)	kf16raw#pro_filtered.mat
17	14		Sinusoid	Rr3	Full	65+65*sin(2π/8.17 t)	kf17raw#pro_filtered.mat
18	15	ROM with small spring	Sinusoid	Rr1	Full	25+25*sin(2π/3.14 t)	kf18raw#pro_filtered.mat
19	16		Sinusoid	Rr2	Full	45+45*sin(2π/5.65 t)	kf19raw#pro_filtered.mat
20	17		Sinusoid	Rr3	Full	65+65*sin(2π/8.17 t)	kf20raw#pro_filtered.mat
21	21	ROM with largest spring	Sinusoid	Rr1	Full	25+25*sin(2π/3.14 t)	kf21raw#pro_filtered.mat
22	22		Sinusoid	Rr2	Full	45+45*sin(2π/5.65 t)	kf22raw#pro_filtered.mat
23	23		Sinusoid	Rr3	Full	65+65*sin(2π/8.17 t)	kf23raw#pro_filtered.mat
24	24	Direct EMU comparison	Human	R-E	Full	From file subject B (Schmidt)	kf24raw#pro_filtered.mat
25	25		Human	R-E	Full	From file subject C (Schmidt)	kf25raw#pro_filtered.mat
26	26		Human	R-E	Full	From file subject E (Schmidt)	kf26raw#pro_filtered.mat
27	27		Sinusoid	R-E	Full	55+55*sin(2π/6.91 t)	kf27raw#pro_filtered.mat
28	28		Sinusoid	R-E	Half	55+55*sin(2π/13.82 t)	kf28raw#pro_filtered.mat

Table 6 - Trajectories corresponding to the test matrix

Description of Test Parameters

Trajectory

Sinusoid: 1 period shown. Each test run was run for about 8 periods (a total time of about 65 seconds). The example below is for an alpha of 65 (i.e., 130/2 = 65). The trajectory is always sinusoidal but the range of motion (i.e., 130, 90, and 50 degrees) is what defines the amplitude of the sine function. The period is adjusted to meet the specified speed.

$$\alpha_m + \alpha_m \cdot \sin(\frac{2\pi}{p} \cdot t)$$
$$\alpha_m = \left|\text{range of motion}\right| / 2$$
$$\text{t} = \text{time (seconds)}$$
$$\text{p} = \text{period (seconds)}$$

Equation 24

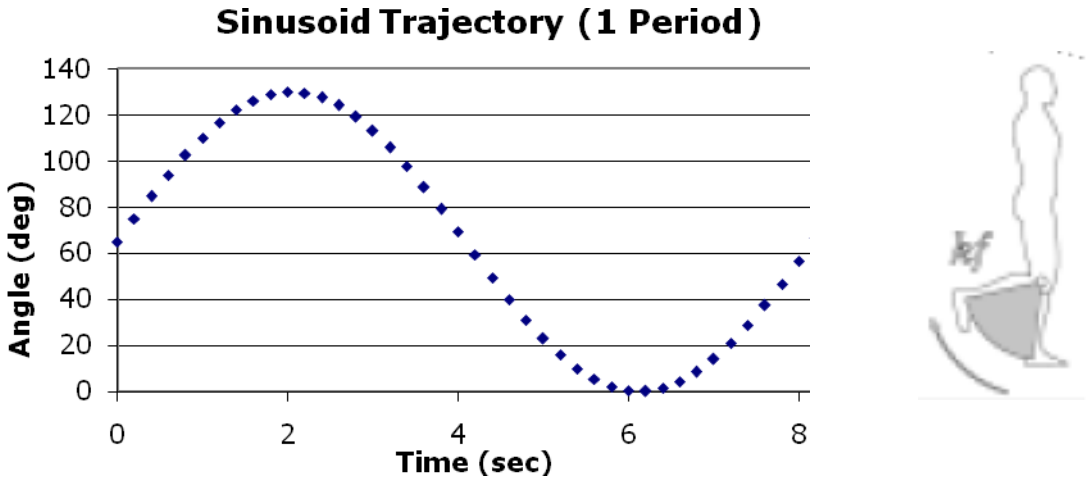

Figure 59 - Description of the sinusoid trajectory

Human: specific to subject's trajectory file. Trajectories from Schmidt subjects B, C, and E were also used.

Speed

Speed was defined as the maximum angular velocity achieved by the joint during a trajectory. This is the derivative of the trajectory (see below). For a given maximum speed (and range of

motion), the period of the sinusoidal trajectory was adjusted in order to take into account the maximum joint speed.

$$\alpha_m \cdot \frac{2\pi}{p} \cdot \cos(\frac{2\pi}{p} t)$$

$$\text{maximum velocity} = \alpha_m \cdot \frac{2\pi}{p}$$

Equation 25

- Full speed: A maximum speed of 50 deg/s was chosen, since this was referenced in Schmidt's thesis. For sinusoid trajectories, this speed was fixed by altering the period of the sinusoid. For human trajectories, the maximum speed was pre-defined by the human trajectory files.
- Half speed: Accordingly, half speed of the joint was set at 25 deg/s.

Range of Motion (ROM) of the Brace

The ROM of the brace was specifically the range that was imposed on the brace:

- R1 = 40° - 90°
- R2 = 20° - 110°
- R3 = 0° - 130°
- R-E = 0° - 110° = range of motion of EMU

Range of Motion (ROM) of the Robot:

This condition was specified to differentiate it from the brace ROM. The ROM of the robot was the angle range that was input to the robot through the trajectory. The sinusoid trajectory (shown above) was for a robot ROM of 0° - 130°. The ranges of motion were the same as those selected for the ROM of brace. *These ranges are pre-determined and not based on testing results.*

- Rr1 = 40° - 90°
- Rr2 = 20° - 110°
- Rr3 = 0° - 130°
- Rr-E = 0° - 110° = range of motion of EMU

Friction

The brace's friction was set by adjusting the brake in two locations, on each side of the brake. Turning screws adjusts the friction level. EMU friction was defined as the standard error of the torque data (processed) if fitted to a linear regression.

- 0 = no applied friction (no tightening of the brakes/remove brake pads)
- 1 = 1.25 Nm (0.25 turn per screw = expected 25% EMU friction)
- 2 = 3.75 Nm (0.75 turns per screw = expected 75% EMU friction)
- 3 = 6.25 Nm (1.25 turns per screw = expected125% EMU friction)
- EMU = 2 (choice made according to the results gathered throughout the testing)

Stiffness

Stiffness was determined by the springs on the knee brace.

- K0 = no spring
- K1 = 4.4 N/mm (short big grey, 25% EMU stiffness)
- K2 = 13 N/mm (skinny grey, 75% EMU stiffness)
- K3 = 20 N/mm (big silver, 110% EMU stiffness)
- K-EMU =K2 (choice made according to the results gathered throughout the testing)

Pre-load

The spring was pre-loaded. There were five possible settings for the pre-load and most conditions were at the center, which was the nominal pre-load setting. The range of the pre-load was examined by testing the extreme pre-load settings, which were the left-most and right-most settings.

EMU comparison

For this comparison, the file **correcteddata.mat** was used (which concatenates the results from three human trajectories: Subject B,C and E [1]), and the knee joint simulator was set to the EMU conditions:

- Spring Stiffness: 13 N/mm
- Smallest Preload
- Friction: 2

Calibration

Before and after each “condition being tested”, the calibration was checked for the robot knee joint. This ensured consistency in our testing methods. This check was done by giving the robot a step input of 45°.

Repeatability

Each of the 28 configurations was tested with three trials unless there was reasonable assurance that the data did not differ across set runs. The order within each set is given on the next page.

To ensure repeatability, ATA also specified torque values for tightening the knee brace bolts, which we adhered to. They were as follows:

- 6mm bolts = 5 ft-lbs
- 8mm bolt = 11 ft-lbs (this is the main axis of rotation)
- All others finger tight = 1 ft-lb

Data Collection

The trial order is specified by Table 6 .To expedite the data collection process, the S3 joint was removed from the robot only after each “set” (3 or 4 conditions within one “condition being tested”). After this, the robot was run without the brace for these same test conditions.

Appendix B: Hysteresis Plots

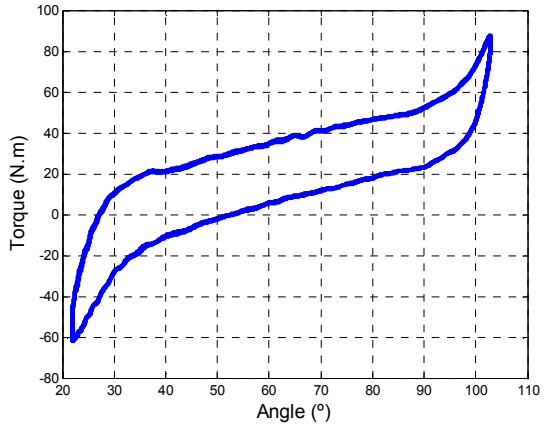

Figure 60 - Hysteresis Plot of Configuration 1

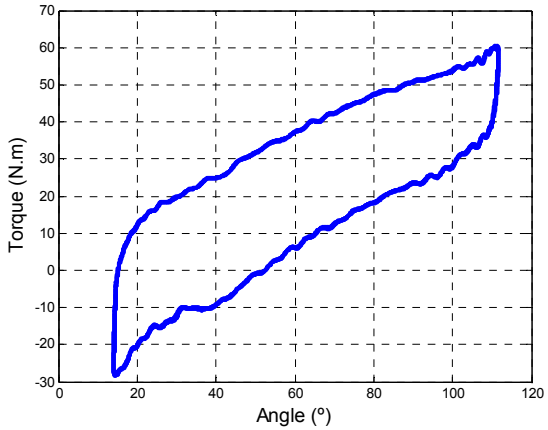

Figure 61 - Hysteresis Plot of Configuration 2

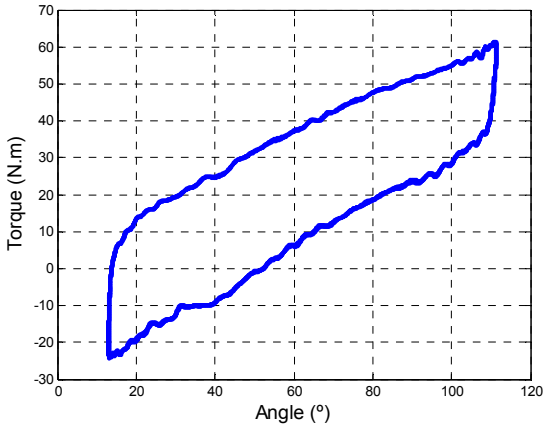

Figure 62 - Hysteresis Plot of Configuration 3

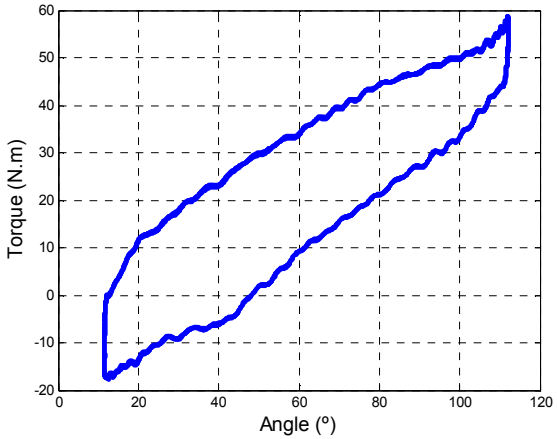

Figure 63 - Hysteresis Plot of Configuration 4

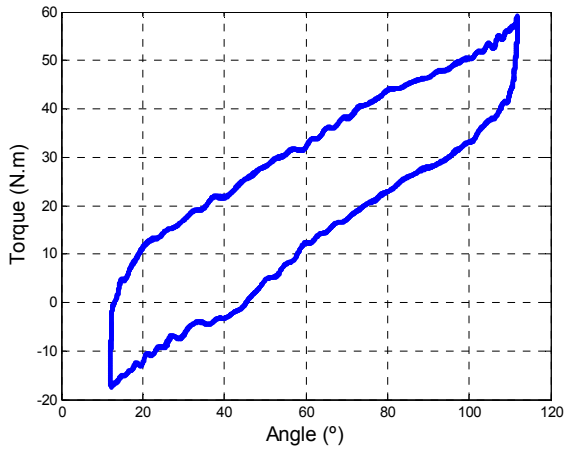

Figure 64 - Hysteresis Plot of Configuration 5

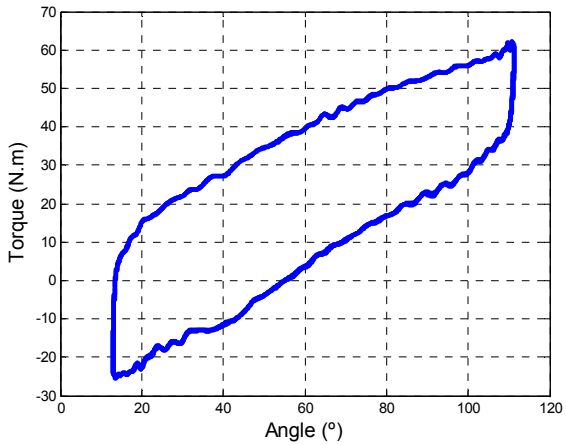

Figure 65 - Hysteresis Plot of Configuration 6

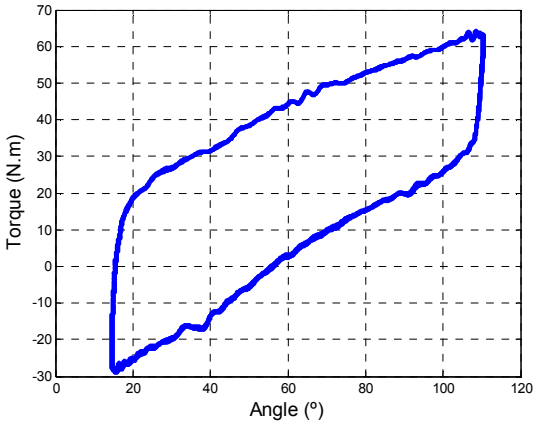

Figure 66 - Hysteresis Plot of Configuration 7

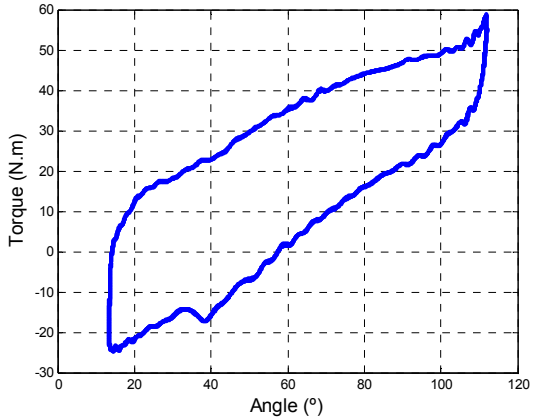

Figure 67 - Hysteresis Plot of Configuration 8

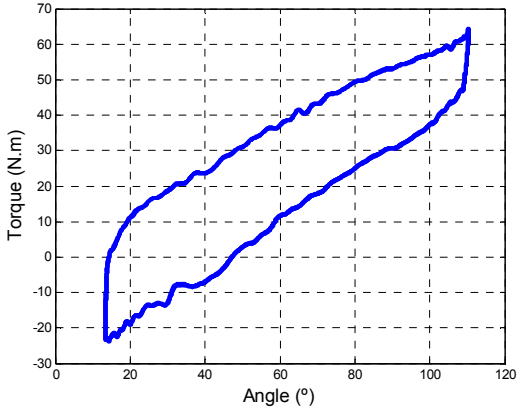

Figure 68 - Hysteresis Plot of Configuration 9

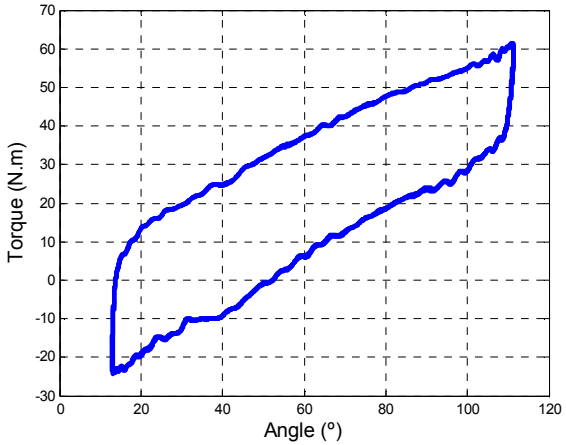

Figure 69 - Hysteresis Plot of Configuration 10

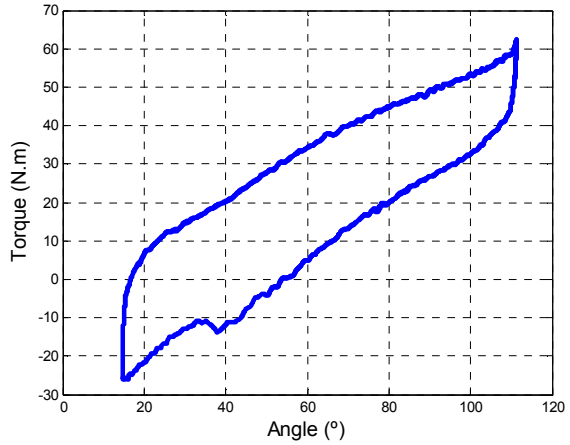

Figure 70 - Hysteresis Plot of Configuration 11

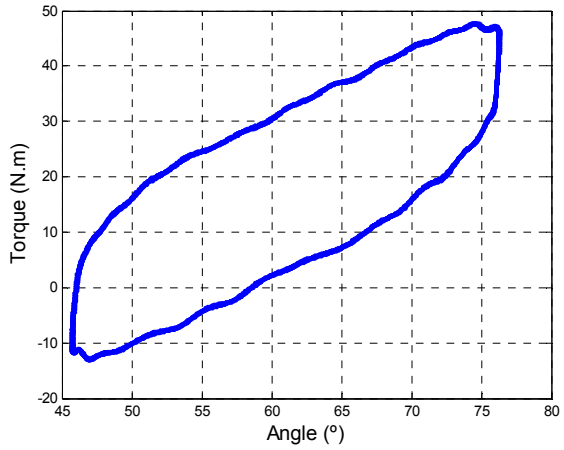

Figure 71 - Hysteresis Plot of Configuration 12

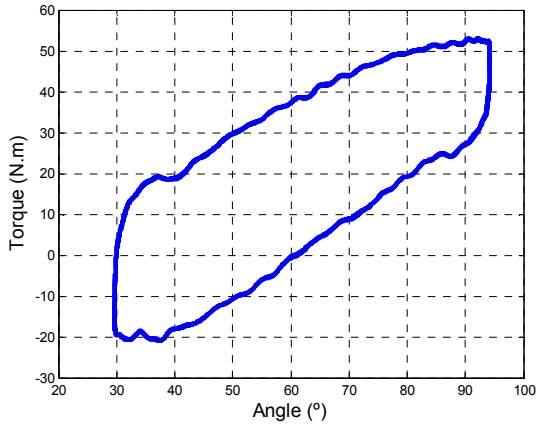

Figure 72 - Hysteresis Plot of Configuration 13

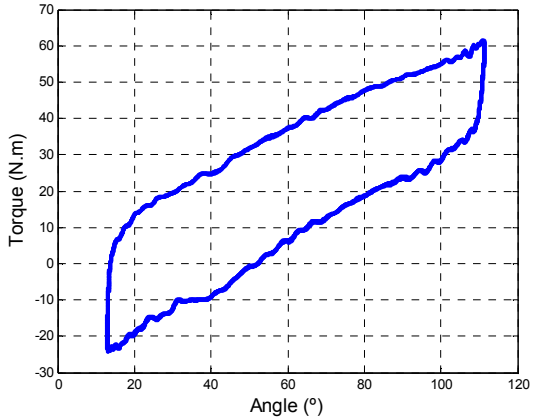

Figure 73 - Hysteresis Plot of Configuration 14

Figure 74 - Hysteresis Plot of Configuration 15

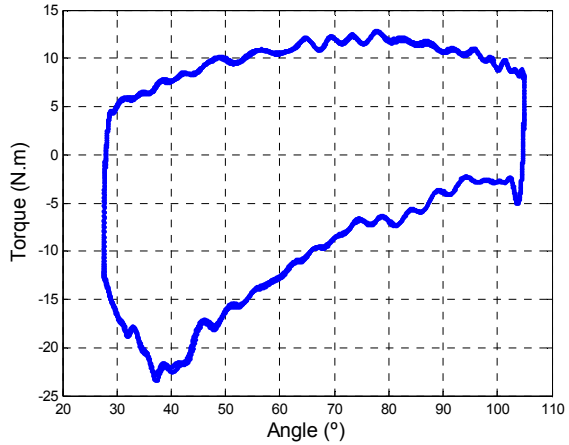

Figure 75 - Hysteresis Plot of Configuration 16

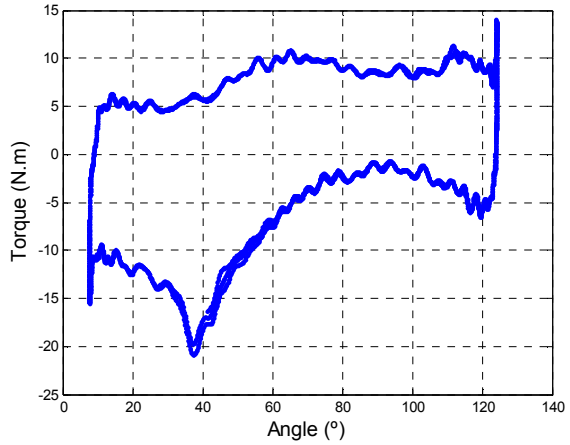

Figure 76 - Hysteresis Plot of Configuration 17

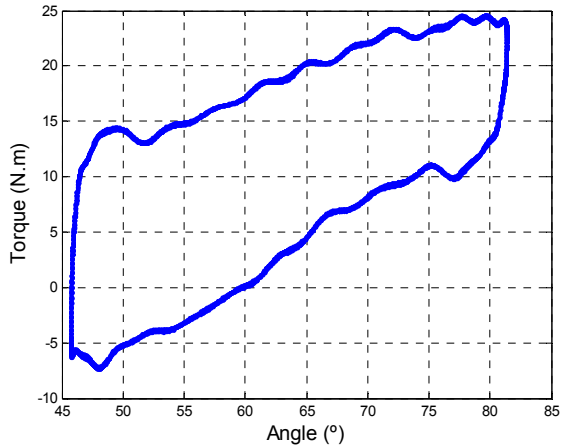

Figure 77 - Hysteresis Plot of Configuration 18

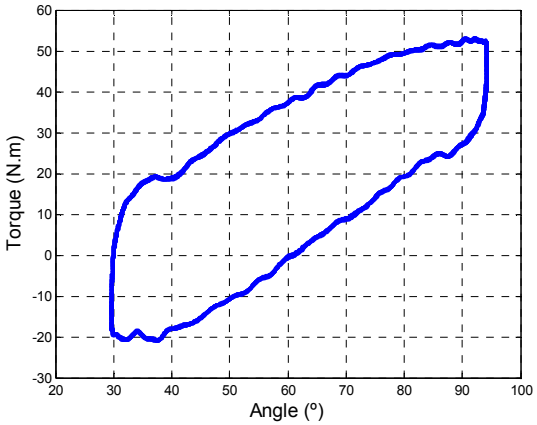

Figure 78 - Hysteresis Plot of Configuration 19

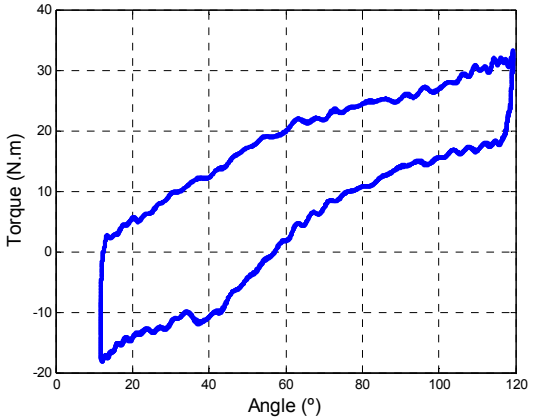

Figure 79 - Hysteresis Plot of Configuration 20

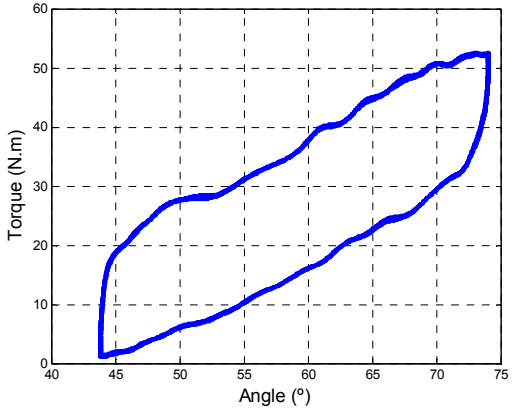

Figure 80 - Hysteresis Plot of Configuration 21

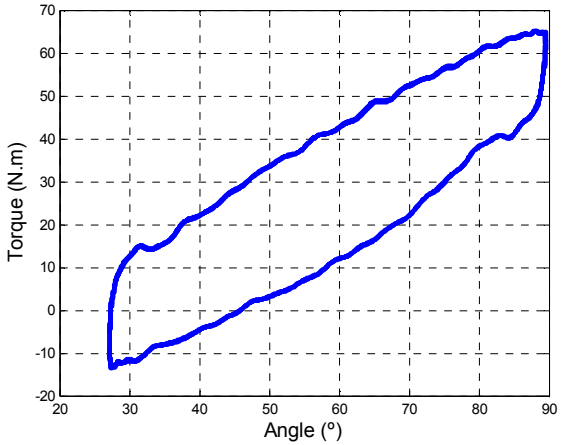

Figure 81 - Hysteresis Plot of Configuration 22

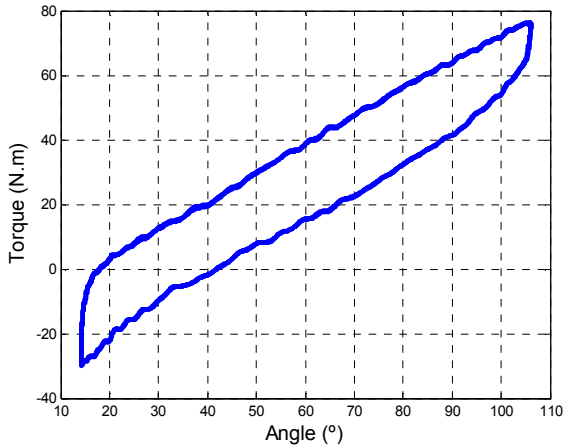

Figure 82 - Hysteresis Plot of Configuration 23

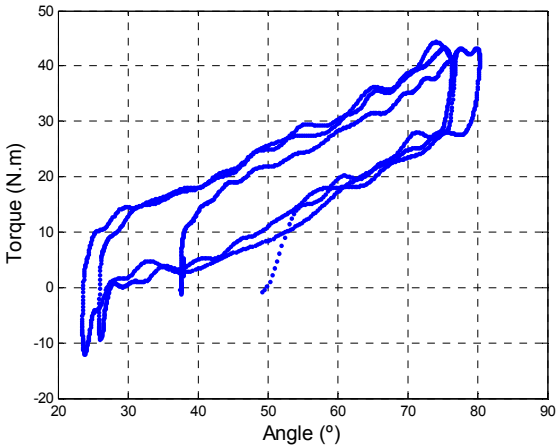

Figure 83 - Hysteresis Plot of Configuration 24

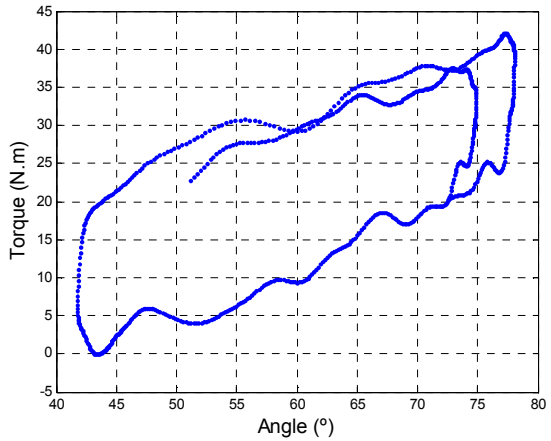

Figure 84 - Hysteresis Plot of Configuration 25

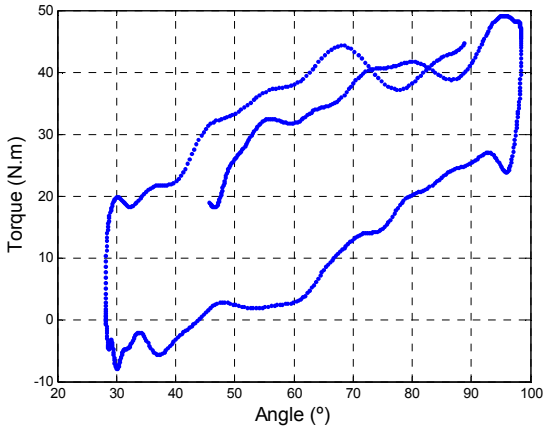

Figure 85 - Hysteresis Plot of Configuration 26

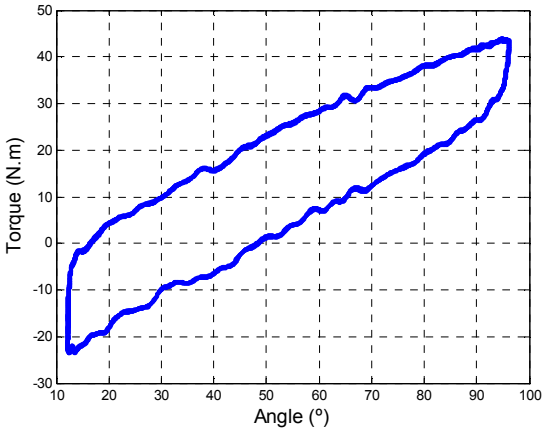

Figure 86 - Hysteresis Plot of Configuration 27

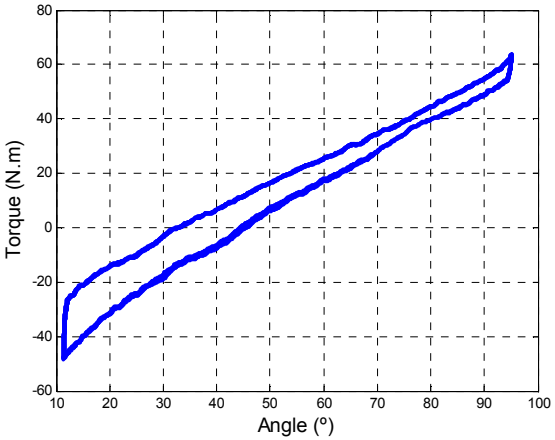

Figure 87 - Hysteresis Plot of Configuration 28

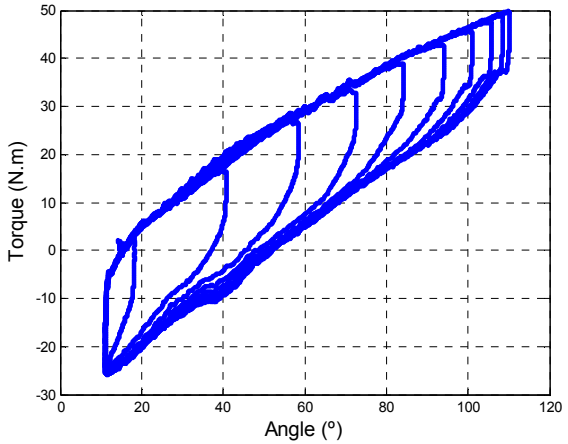

Figure 88 -Hysteresis Plot of Extra Configuration 1

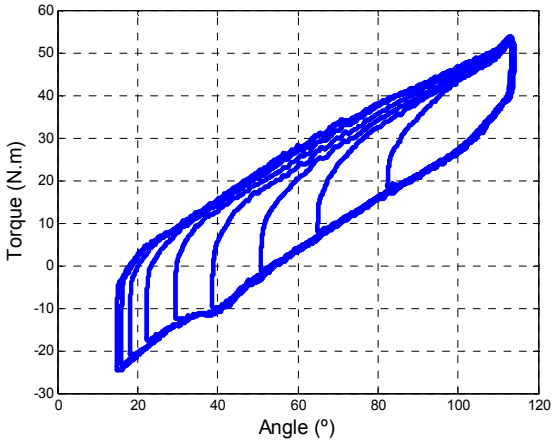

Figure 89-Hysteresis Plot of Extra Configuration 2

Note: Two extra trials were done to shown a trajectory of loops going up and loops going down (Figure 88 and Figure 89, respectively)